Studies on Vapochromic Behaviors of Supramolecular Pt(II) Complexes with Porous Structures

（多孔性超分子白金(II)錯体のベイポクロミズムに関する研究）

Yasuhiro Shigeta

Graduated School of Chemical Sciences and Engineering
Hokkaido University
2018

Contents

Chapter 1

General Introduction

1-1 Introduction -2-
1-2 Vapochromism
1-2-1 General remarks on Vapochromism -3-
1-2-2 Type I Vapochromic materials: Vapochromism based on metallophilic interactions -4-
1-2-3 Type II vapochromic materials: Vapochromism by direct bonding between chromophores and vapor molecules -7-
1-2-4 Type III vapochromic materials: Vapochromism by indirect interaction between chromophore and guest molecule -9-
1-3 Vapochromism on porous materials -10-
1-4 Purpose of the thesis -12-
1-5 Outline of the thesis -15-
1-6 References -16-

Chapter 2

"*Shape-Memory" Platinum(II) Complexes: Intelligent Vapor-History Sensor with ON–OFF Switching Function*

2-1 Introduction -19-
2-2 Experimental section
2-2-1 Materials, synthesis and sample preparation -21-
2-2-2 Physical measurements -22-
2-3 Results and discussion
2-3-1 Crystal structures -23-
2-3-2 Multichromism -26-
2-3-3 "Molecular-scale shape-memory effect" and ON–OFF switching of the vapochromism -36-
2-3-4 Thermochromic luminescence -46-
2-4 Conclusion -49-
2-5 References -50-

Chapter 3

Vapochromic Pt(II) Complexes Having Vapor-History Sensing Ability

3-1 Introduction -52-

3-2 Experimental section

3-2-1 Materials and synthesis -54-

3-2-2 Physical measurement -55-

3-3 Results and discussion

3-3-1 Synthesis and Characterization -56-

3-3-2 Crystal structure of $[Pt(CN)_2(H_2dpcpbpy)]\cdot 3H_2O$(**3-Oc**) -58-

3-3-3 Vapor-adsorption-triggered structure transformation -62-

3-3-4 Vapochromism -67-

3-4 Conclusion -75-

3-5 References -77-

Chapter 4

General Conclusion -79-

Acknowledgement -81-

Chapter 1

General Introduction

1-1 Introduction

Smart materials, which have a switching function changed by some external stimuli, have attracted considerable attention because these materials are able to detect the external stimulus and respond by switching its function.[1)] Generally, the following three components are required to design an external-stimuli-responsive machine.

1: The component to detect external stimulus

2: The component to response to the external stimulus

3: Connecting part to couple the functions of 1 and 2

Although such functions can be designed by normal electric devices (e.g., a machine built from the combination of an electric sensor and a display), molecular smart materials have been also developed recently because they have lots of potentials for miniaturization and energy saving of machines.

Chromism is a phenomenon of reversible color change caused by external stimulus and counted as one of promising properties for smart materials.[2)] Up to now, many kinds of stimuli-responsive chromic materials have been reported. Chromic materials are classified and named by responding stimulus using as prefix. For example, temperature (thermochromism), light[3)] (photochromism) and electricity[4)] (electrochromism) has reported as detectable stimulus. Chromic materials can be utilized as sensors because these materials visualize external stimulus as its color.

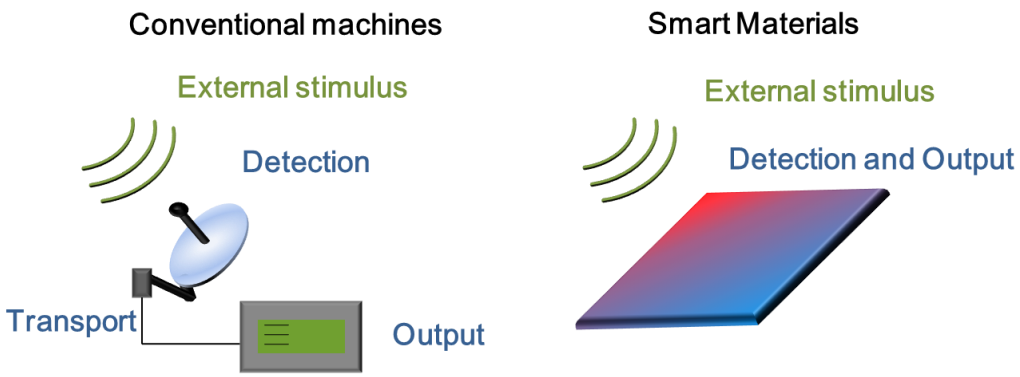

Figure 1-1. Schematic images of conventional machines and smart materials which detect external stimulus.

1-2 Vapochromism

1-2-1 General remarks on vapochromism

Vapochromism, one of chromisms, is a phenomenon of reversible color changes induced by vapor exposure. This behavior enables us to know the existence of invisible harmful volatile organic compounds (VOCs) as the color changes of the material. Thus, vapochromic materials are good candidates for the chemical sensors and have been much studied so far.[5] The word, "vapochromism" was firstly used by C. C. Nagle, in his patent on 1988.[6] They synthesized the double salt composed by square-planar type Pt(II) and Pd(II) complexes and reported that the salt exhibited color change from deep-pink to blue upon in the presence of chloroform vapor.

In the research field of vapochromism, the following three types of mechanisms have been studied (Figure 1-2).[7]

Type I: Inter- or intra-molecular interaction changes induced by vapor

Type II: Direct bonding between chromophore and vapor molecule

Type III: Weak π-π and/or CH···π interactions between chromophore and vapor molecule

Among them, major part for research on vapochromism was occupied by Types I and II. Transition metal complexes were widely used in almost of all Type I and Type II vapochromic materials, because of unique functions originated from their d orbitals. Details are described in the following sections.

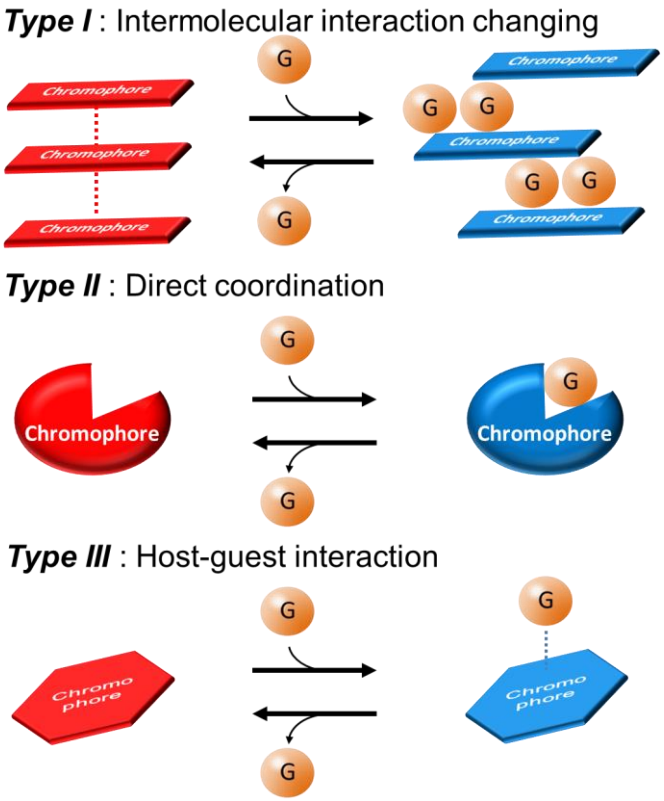

Figure 1-2. Three-types mechanisms of vapochromism.

1-2-2 Type I vapochromic materials: Vapochromism based on metallophilic interactions

Type I vapochromic behavior is originated from inter- or intra-molecular interactions and most of vapochromic materials are classified into this type. The transition metal ions with d^8 or d^{10} electron configuration are widely used for this type of vapochromic materials. Especially, Pt(II)[8] and Au(I)[9] ions are extensively studied so far. These metal complexes tend to form one-dimensionally stacked structure in the solid state because of the effective orbital overlap between the occupied $5d_z^2$ and vacant $6p_z$ orbitals. These intermolecular orbital overlaps generate intermolecularly delocalized electronic orbitals, that is, the occupied dσ* orbital and the empty pσ orbital, and the electronic transition between them is usually observed (Figure 1-3). In the system with π orbital in the ligands, electron transition from the dσ* orbital to π* orbital of the ligand, so called Metal-Metal-to-Ligand Charge Transfer (MMLCT) transition, is also observed. The transition energy highly depends on the magnitude of the intermolecular orbital overlap, that is, the metallophilic interactions. It is possible to estimate whether the metallophilic interaction between these metal ions is effective or not by comparing the distance between two adjacent metal ions. If the distance is shorter than sum of the van der Waals radius of the metals, metallophilic interaction would be effective. For example, in case of Pt(II) complexes, threshold for the metallophilic interaction can be estimated at 3.5 Å which is twice of van der Waals radius of Pt metal (1.75 Å).

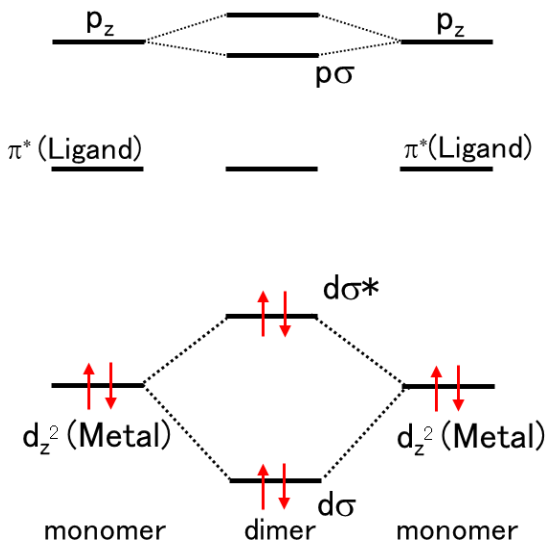

Figure 1-3. Schematic energy diagram derived from the metallophilic interaction between two square-planar Pt(II) complexes.

In the context, Connick and co-workers reported the relationship between Pt-Pt interaction and luminescence energy of the red form of Pt(II) complex, $[PtCl_2(bpy)]$.[10] They found a linear relationship between the R^{-3} (R = intermolecular Pt-Pt distance in the one-dimensionally stacked structure) and the ^{3}MMLCT emission energy, indicating that the intermolecular Pt-Pt distance gives a crucial effect on the emission energy (Figure 1-4). Notably, only the small modification (~0.08 Å) of the intermolecular Pt-Pt distance change can induce the large change of the emission energy (~1000 cm^{-1} from 613 to 651 nm). The same trend was also reported for the other one-dimensionally stacked Pt(II) complexes by Day[11], Kato[12] and their co-workers.

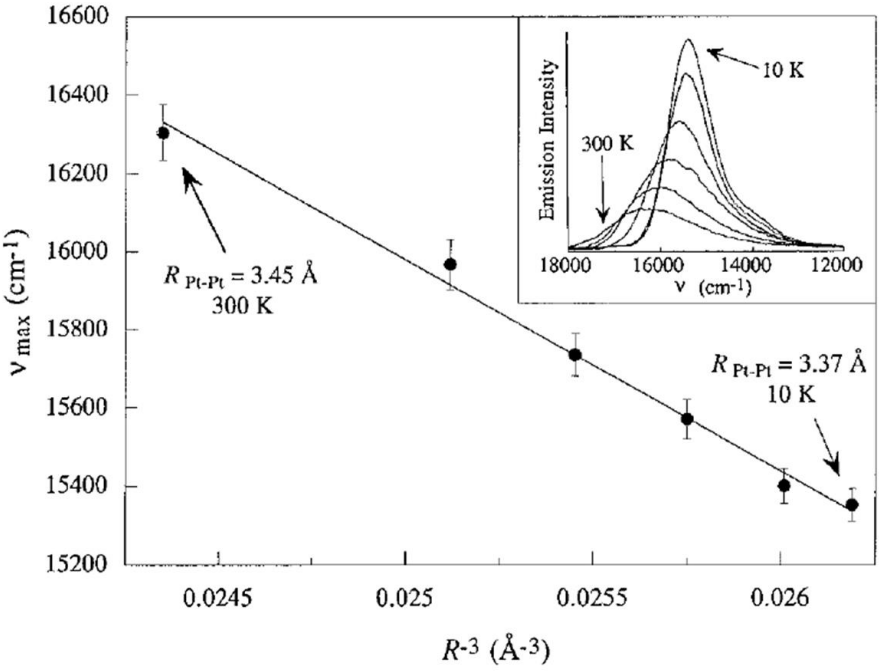

Figure 1-4. Relationship between emission maximum energy and inverse cube of the Pt-Pt distances (R^{-3}).

Type I vapochromic materials were extensively studied in 2000s by W. B. Connick,[13] R. Eisenberg[14] and K. R. Mann.[15] Especially, Eisenberg and co-workers reported the vapochromism of $[PtCl(Nttpy)](PF_6)$ (Nttpy = 4'-(*p*-nicotinamide-N-methylphenyl)-2,2':6',2''-terpyridine) based on single crystal X-ray diffraction study (Figure 1-5).[14a] This complex exhibited single-crystal to single crystal transformation from the MeOH-included form to the MeOH-removed form. The intermolecular Pt-Pt distances of the MeOH-included form were estimated to be 3.6614(5) Å and 4.0384(5) Å.

Since these values are longer than twice of van der Waals radius (3.5 Å), the metallophilic interaction is not effective. On the other hand, after standing overnight at ambient temperature, the color was changed from orange to red with retaining its crystallinity. Single crystal X-ray diffraction measurement revealed that the Pt-Pt distances in this red form is estimated at 3.3009(7) Å and 3.3644(8) Å which clearly indicates that the metallophilic interactions are effective. This Pt-Pt interaction difference affected to luminescence spectrum. Orange form exhibited yellow luminescence derived from the triplet Metal to Ligand Charge Transfer (^{3}MLCT) transition state because of the negligible Pt-Pt interaction. In contrast, the red form exhibited ^{3}MMLCT emission generated by the effective Pt-Pt interaction.

These typical examples mentioned above clearly indicate that the Type I mechanism is promising for the vapochromic behavior because even a very small change in the intermolecular interaction could be detected as a large change in emission/absorption energy.

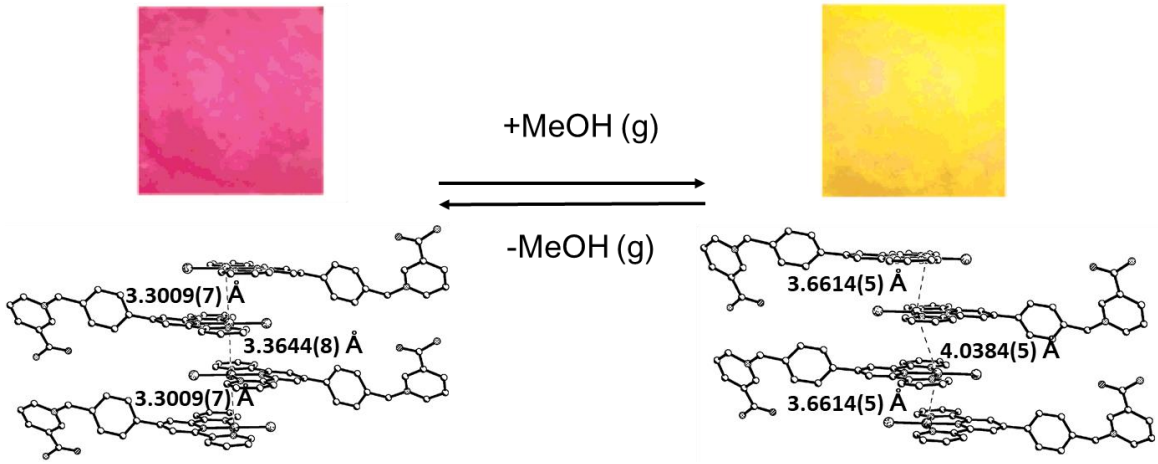

Figure 1-5. Emission color images and one-dimensionally stacked structures of the MeOH included (left) and MeOH-removed (right) forms.

1-2-3 Type II vapochromic materials: Vapochromism by direct bonding between chromophores and vapor molecules

As mentioned above, Type II mechanism is based on the direct bonding between chromophores and vapor molecules. This type vapochromic materials are mainly reported on 3d transition metal complexes, for example, Co(II)[16], Ni(II)[17], Cu(I)[18] and Cu(II)[19]. Since these 3d transition metal complexes are intrinsically labile, the ligands can be easily substituted by solvent molecules. This labile nature is the key for the Type II vapochromic materials. The ligand field splitting of the metal center significantly changed by the coordination of vapor molecule, resulting in the significant color change. These properties of 3d metal complexes enable them to exhibit Type II vapochromism.

For example, Baho and co-workers reported that [Ni(dpdpm)(η^2-NO_3)$_2$] (dpdpm = diphenyl(dipyrazolyl)methane) exhibited color change from blue to green under exposure to acetonitrile vapor (Figure 1-6).[17b] Single crystal X-ray structural analysis and absorption spectrum measurement revealed that this behavior is originated from dissociation of one of the oxygen atoms in the NO_3^- ligand and the coordination of acetonitrile vapor.

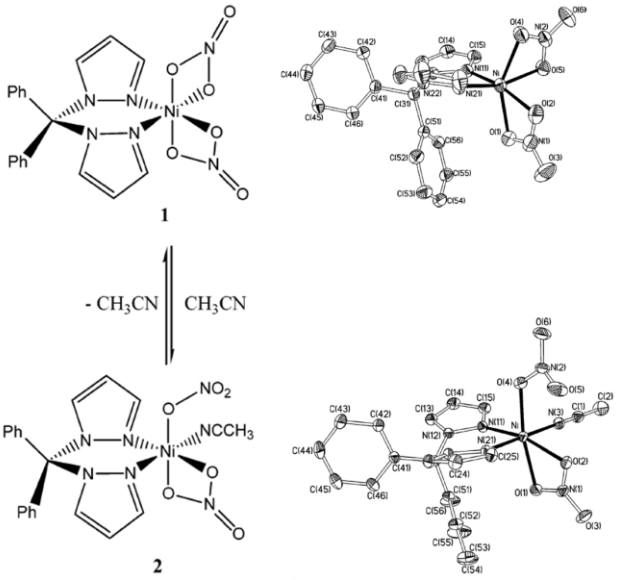

Figure 1-6. Molecular structures and ORTEP diagrams for the CH_3CN-adsorbed (top) and CH_3CN-desorbed (bottom) forms.

Recently, Kar and co-workers reported an interesting vapochromic behavior of [Ni(HLMe)$_2$] (H_2LMe=4-methylamino-6-methyliminio-3-oxocyclohexa-1,4-dien-1-olate), which coupled with the spin-state switching of Ni(II) center.[17c] This Ni(II) complex transformed from the purple-colored square-planar geometry to the orange-colored methanol-coordinated octahedral geometry by adsorption of methanol vapor. Upon this changing, the spin state of Ni(II) center changed from paramagnetic to diamagnetic (Figure 1-7). After removal of the methanol by heating, the complex exhibited paramagnetic behavior again.

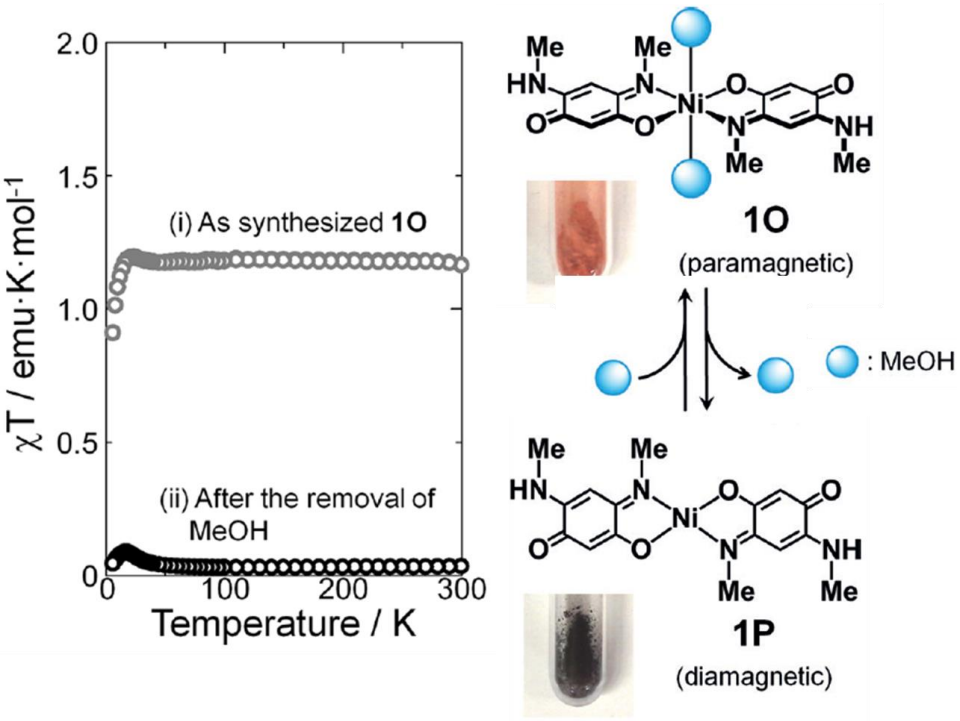

Figure 1-7. Temperature dependence of χT (left) and reversible color change of the complex (right).

As mentioned above, coordination of vapor molecule to the central metal ion is the key factor in the Type II vapochromism. Although the strategy for vapor accessing into the inside of the crystal is required to exhibit vapochromism, Type II mechanism enables us to “design” vapochromic materials to some extent by changing metal center and analyte.

1-2-4 Type III vapochromic materials: Vapochromism by indirect interaction between chromophore and guest molecule

Type III vapochromism is based on indirect interaction between chromophore and guest molecule such as π-π, CH···π and hydrogen bonding.[20] The origins of color change are varied in this mechanism.

For example, Bao and co-workers reported that $[Fe(tpa)(NCS)_2]$ (tpa = tris(2-pyridylmethyl)amine) exhibited methanol vapor induced color change from yellow to red (Figure 1-8).[20] They revealed that this vapochromism originated from spin crossover behavior by single crystal X-ray structural analysis, magnetic measurements and Mössbauer spectroscopy. The crystal of yellow form was composed of only one crystallographically independent high-spin (HS) state Fe(II) complex at room temperature. In contrast, the red crystal obtained by exposure to methanol vapor was composed of two crystallographically independent HS and low spin (LS) state Fe(II) complexes at room temperature. The authors concluded that this spin crossover behavior is probably due to the hydrogen bonding between NCS ligand and the adsorbed methanol vapor that *indirectly* affected the ligand-field splitting of the Fe(II) center.

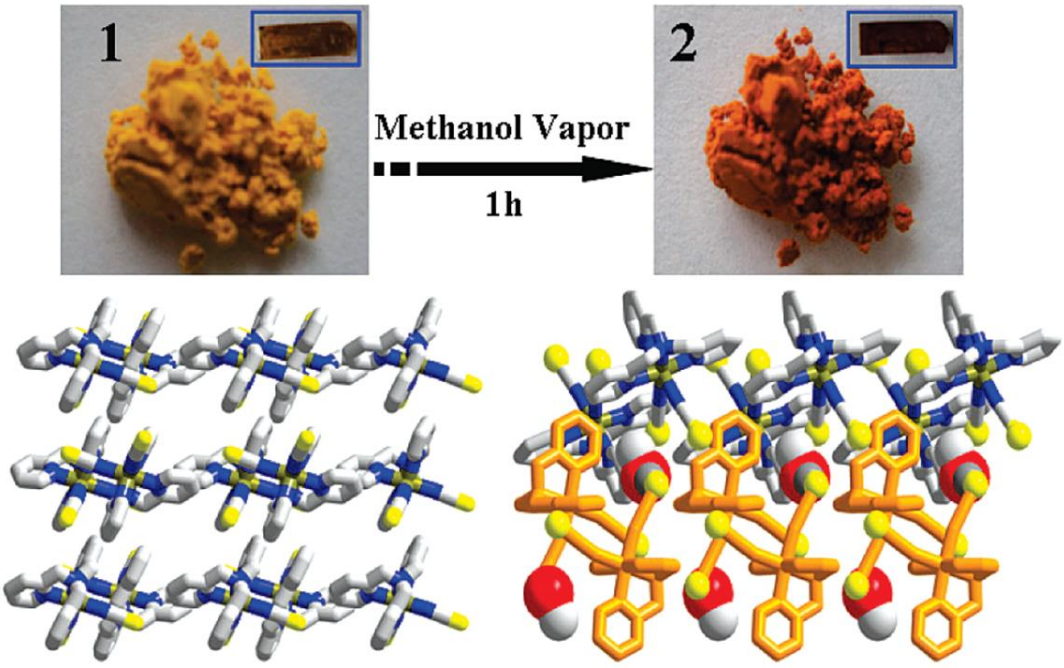

Figure 1-8. MeOH vapor induced color change (top images) and crystal packings of the MeOH desorbed form (left) and adsorbed form (right).

1-3 Vapochromism for porous materials

As mentioned above, most of the vapochromic materials can be classified to Type I. This is probably due to the metallophilic interaction is sensitive enough to detect small structural change induced by the external stimulus. However, to design a vapochromic material based on the Type I mechanism is still difficult. This is because both the control of crystal structure and vapor adsorption behavior are required. In other words, the vapor accessible site is necessary to recognize the vapor molecule, and the vapor adsorption is required to induce color change of the chromophore. From the viewpoint of the vapor adsorption site, porous materials are promising candidate to design vapochromism[21]. Metal-Organic Frameworks (MOFs) with nano-sized pores are promising materials for vapochromism, because they are well-known to adsorb vapor molecule by its porous nature.[22]

For example, the vapochromic and solvatochromic behaviors of $\{[(WS_4Cu_4)\text{-}I_2(dptz)_3]\cdot DMF\}_n$ (dptz = 3,6-dipyridin-4-yl-1,2,4,5-tetrazine) has been reported by Lu and co-workers.[21c] This MOF can be obtained as the DMF-adsorbed form, but the DMF molecules can be replaced by heating and subsequently immersing to the other solvent (Figure 1-9). In this solvent exchanging process, MOF exhibited color change depends on the immersed solvent. This behavior can also be slowly observed under exposure to solvent vapors, and a certain blue-shift was observed in the UV-Vis absorption spectrum by increasing solvent polarity. This color change was not observed for the bpy-bridged analogue MOF, $\{[WS_4Cu_4(4,4'\text{-bpy})_4][WS_4Cu_4(4,4'\text{-bpy})_2I_4]\}_n$ (4,4'-bpy = 4,4'-bipyridine). The authors finally concluded that the vapochromic and solvatochromic behaviors of this MOF originated from the interaction between the bridging dptz ligand and adsorbed solvent molecules based on the strong π-accepting nature of dptz ligand. Therefore, porous materials are promising material for the vapochromic materials which can detect various vapors by physisorption into the opened pores. This approach has been widely utilized for Type II and Type III vapochromic materials, because these mechanisms are basically based on the interaction between chromophores and vapor molecules.–

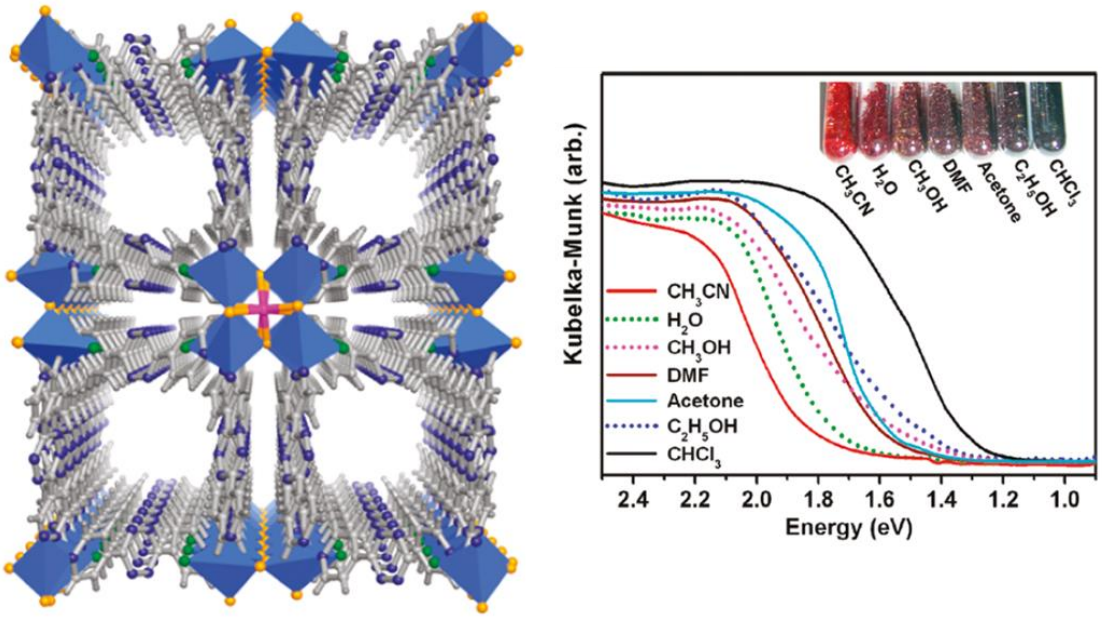

Figure 1-9. Porous structure of $\{[(WS_4Cu_4)\text{-}I_2(dptz)_3]\cdot DMF\}_n$ (left) and diffuse reflectance spectra and photographs of various solvent-included forms.

1-4 Purpose of the thesis

Although porous materials are good candidate for vapochromic material as discussed in the previous section, there is few reports for applying the porosity to the Type I vapochromic behavior. This might be due to the energy difference between the metallophilic interactions and ionic and/or coordination bonding interactions. Most of the Type I vapochromic materials are basically molecular crystals constructed by weak intermolecular interaction. In contrast, MOFs are constructed by relatively strong ionic and/or coordination bonds. Therefore, such a strong ionic and/or coordination bonding interaction might suppress formation of the intermolecular metallophilic interactions.

Type I vapochromic coordination polymer (CP), {Zn[Pt(CN)$_2$(5,5'-dcbpy)]} (5,5'-H$_2$dcbpy = 5,5'-dicarboxy-2,2'-bipyridine) has been reported by Kobayashi and co-workers.[23] This one-dimensional CP was constructed by bridging Zn(II) ions and carboxylic-acid-functionalized Pt(II)-diimine metalloligands (Figure 1-10). This one-dimensional coordination chains were stacked to make the Pt-Pt interaction effective. This coordination polymer exhibited vapochromic and solvatochromic behaviors originated from the modification of the Pt-Pt interaction induced by the hydration number changes of the Zn(II) center.

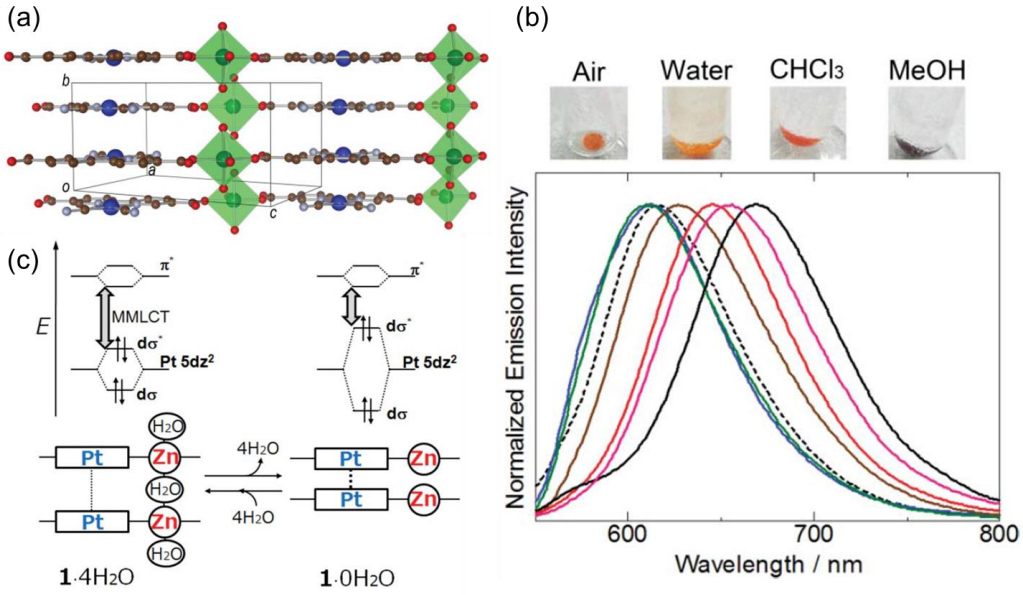

Figure 1-10. (a) Packing diagram for the {Zn[Pt(CN)$_2$(5,5'-dcbpy)]} (b) Bright field images and emission spectra of soaked complex various liquid media (c) Possible mechanism of the chromic behavior.

Moreover, Kato and co-workers reported porous Type I vapochromic Pt(II) complex, $[Pt(CN)_2(H_2dcbpy)]$ (Scheme 1-1; **1**; H_2dcbpy = 4,4'-dicarboxy-2,2'-bipyridine).[24] In spite of the absence of strong bonding such as ionic bond, this complex was reported to form a porous structure constructed by intermolecular hydrogen bonding and Pt-Pt interactions (Figure 1-11). This vapochromism is based on the amorphous-crystalline transformation induced by high polarity vapor molecule such as methanol.[25] Thus, relatively weak hydrogen bonding enables to cope with both Type I mechanism and porous crystal structure.

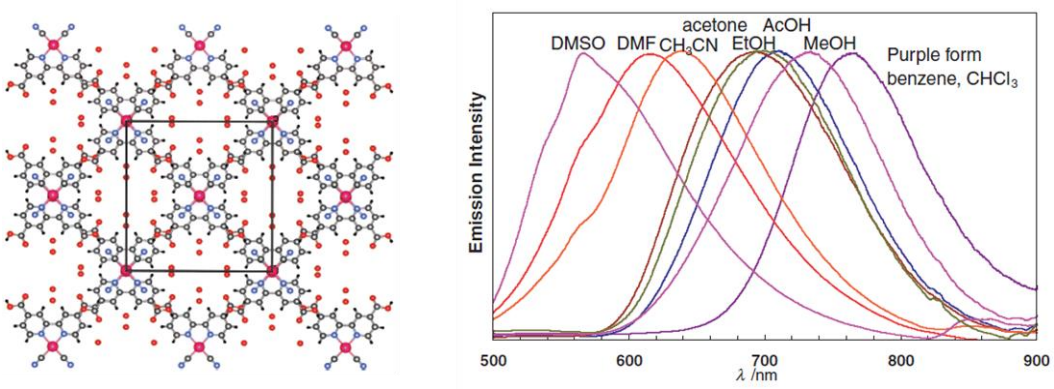

Figure 1-11. Packing diagram of $[Pt(CN)_2(H_2dcbpy)]$ (left, porous red form) and luminescence spectral changes for amorphous purple form.

In this thesis, to examine the detail of the Type I vapochromism with porous structure constructed by hydrogen bonding, previously reported $[Pt(CN)_2(H_2dcbpy)]$ was systematically modified and the vapochromic behavior changing was investigated. Type I mechanism should enable to recognize slightly different crystal structures by its sensitivity. Moreover, relatively weak, flexible hydrogen bonding should allow forming various crystal structures.

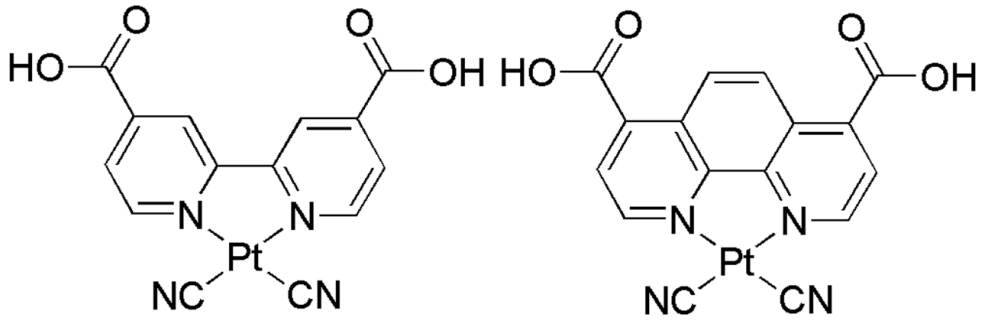

Complex 1
[$Pt(CN)_2(H_2dcbpy)$]

Complex 2
[$Pt(CN)_2(H_2dcphen)$]

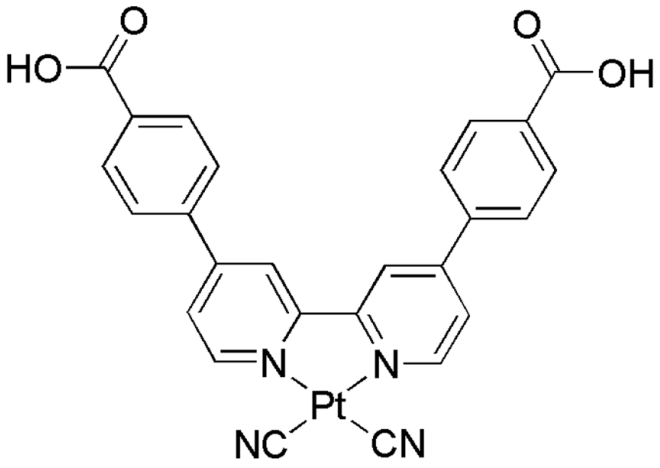

Complex 3
[$Pt(CN)_2(H_2d$*p*$cpbpy)$]

Scheme 1-1. Molecular structures of **1**, **2** and **3**.

1-5 Outline of the thesis

This thesis consists four chapters as described below.

In chapter 1, the research background and purpose of this thesis were described. Especially, the three different mechanisms for vapochromism were described to figure out the design strategies for vapochromic materials. Several advantages of porous materials such as metal-organic frameworks for vapochromic behavior are also discussed.

In chapter 2, the synthesis, crystal structure and vapochromic behavior of complex **2**, $[Pt(CN)_2(H_2dcphen)]$ ($H_2dcphen$ = 4,7-dicarboxy-1,10-phenanthroline) were described and compared to the vapochromic behavior of previously reported complex, $[Pt(CN)_2(H_2dcbpy)]$ (H_2dcbpy = 4,4'-dicarboxy-2,2'-bipyridine). The vapor size dependence of vapochromism is discussed based on X-ray diffraction (XRD) and luminescence measurements. Moreover, these complexes were found to exhibit unique "molecular-scale shape-memory effect" in the vapochromic process. Vapor adsorption isotherm measurements were also conducted to reveal the detail of the "molecular-scale shape-memory effect".

In chapter 3, the synthesis, crystal structure and its vapochromic behavior of complex **3**, $[Pt(CN)_2(H_2dpcpbpy)]$ ($H_2dpcpbpy$ = 4,4'-di-(*p*-carboxy)- 2,2'-bipyridine) were described and compared to those of complex **2**. XRD and vapor adsorption isotherm measurements were conducted to discuss the stability of porous crystal structures of **2** and **3**. The relationship between the crystal structure and luminescence property was also studied in detail.

In chapter 4, general conclusion and future perspective are described.

1-6 References

(1) a) A. Lendlein and S. Kelch, *Angew. Chem. Int. Ed.*, **2002**, *41*, 2034-2057. b) T. Ikeda, J.-I. Mamiya and Y. Yu, *Angew. Chem. Int. Ed.*, **2007**, *46*, 506-528. c) T. R. Shrout and S. J. Zhang, *J. Electroceram.*, **2007**, *19*, 111-124.

(2) W. Linert., Y. Fukuda and A. Camard, *Coord. Chem. Rev.*, **2001**, *218*, 113-152.

(3) a) M. Irie, *Chem. Rev.*, **2000**, *100*, 1685-1716. b) S. Kawata and Y. Kawata, *Chem. Rev.*, **2000**, *100*, 1777-1788.

(4) P. M. Beaujuge and J. R. Reynolds, *Chem. Rev.*, **2010**, *110*, 268-320.

(5) O. S. Wenger, *Chem. Rev.*, **2013**, *113*, 3686-3733.

(6) C. C. Nagle, U. S. Patent No. 4826774

(7) A. Kobayashi, Y. Fukuzawa, H.-C. Chang, and M. Kato, *Inorg. Chem.,* **2012**, *51*, 7508−7519.

(8) a) C. L. Exstrom, J. R. Sowa, Jr., C. A**.** Daws, D. Janzen, and K. R**.** Mann, *Chem. Mater.*, **1995**, *7*, 15-17. b) C. A. Daws, C. L. Exstrom, J. R. Sowa, Jr., and K. R. Mann, *Chem. Mater.*, **1997**, *9*, 363-368. c) M. Kato, A. Omura, A. Toshikawa, S. Kishi, and Y. Sugimoto, *Angew. Chem. Int. Ed.*, **2002**, *41*, 3183-3815. d) S. C. F. Kui, S. S.-Y. Chui, C.-M. Che, and N. Zhu, *J. Am. Chem. Soc.*,**2006**, *128*, 8297-8309. e) J. Fornie´s, S. Fuertes, J. A. López, A. Martı´n, and V. Sicilia, *Inorg. Chem.*, **2008**, *47*, 7166-7176. f) M. L. Muro, C. A. Daws and F. N. Castellano, *Chem. Commun.*, **2008**, 6134–6136. g) J. Ni, X. Zhang, Y.-H. Wu, L.-Y. Zhang, and Z.-N. Chen, *Chem. Eur. J.*, **2011**, *17*, 1171-1183. h) A. Kobayashi, H. Hara, T. Yonemura, H.-C. Chang and M. K., *Dalton Trans.*, **2012**, *41*, 1878-1888. i) A. Han, P. Du, Z. Sun, H. Wu, H. Jia, R. Zhang, Z. Liang, R. Cao and R. Eisenberg, *Inorg. Chem.*, **2014**, *53*, 3338-3344.

(9) a) M. A. Mansour, W. B. Connick, R. J. Lachicotte, H. J. Gysling, and R. Eisenberg, *J. Am. Chem. Soc.* **1998,** *120,* 1329-1330. b) J. Lefebvre, R. J. Batchelor, and D. B. Leznoff, *J. Am. Chem. Soc.*, **2004**, *126*, 16117-16125. c) R. L. White-Morris, M. M. Olmstead, S. Attar, and A. L. Balch, *Inorg. Chem.*, **2005**, *44*, 5021-5029. d) S. H. Lim, M. M. Olmstead and A. L. Balch, *Chem. Sci.*, **2013**, *4*, 311–318.

(10) W. B. Connick, L. M. Henling, R. E. Marsh, and H. B. Gray, *Inorg. Chem.,* **1996**, *35*, 6261-6265.

(11) P. Day, *J. Am. Chem. Soc.,* **1975***, 97*, 1588-1589.

(12) M. Kato, C. Kosuge, K. Morii, J. S. Ahn, H. Kitagawa, T. Mitani, M. Matsushita, T. Kato, S. Yano and M. Kimura, *Inorg. Chem.*, **1999**, *38*, 1638-1641.

(13) a) L. J. Grove, J. M. Rennekamp, H. Jude, and W. B. Connick, *J. Am. Chem. Soc.*, **2004**, *126*, 1594-1595. b) L. J. Grove, A. G. Oliver, J. A. Krause, and W. B. Connick, *Inorg. Chem.*, **2008**, *47*,1408-1410.

(14) a) T. J. Wadas, Q.-M. Wang, Y.-J. Kim, C. Flaschenreim, T. N. Blanton, and R. Eisenberg,

J. Am. Chem. Soc., **2004**, *126*, 16841-16849.

b) P. Du, J. Schneider, W. W. Brennessel, and R. Eisenberg, *Inorg. Chem.*, **2008**, *47*, 69-77.

(15) a) C. E. Buss and K. R. Mann, *J. Am. Chem. Soc.*, **2002**, *124*, 1031-1039. b) A. G. Dylla, D. E. Janzen, M. K. Pomije, and K. R. Mann, *Organometallics*, **2007**, *26*, 6243-6247. c) S. M. Drew, L. I. Smith, K. A. McGee, and K. R. Mann, *Chem. Mater*, **2009**, *21*, 3117-3124.

(16) a) L. G. Beauvais, M. P. Shores, and J. R. Long, *J. Am. Chem. Soc.*, **2000**, *122*, 2763-2772. b) J. Boonmak, M. Nakano, N. Chaichit, C. Pakawatchai and S. Youngme, *Dalton Trans.*, **2010**, *39*, 8161-8167.

(17) a) E. Y. Lee and M. P. Suh, *Angew. Chem. Int. Ed.,* **2004**, *43*, 2798-2801. b) N. Baho and D. Zargarian, *Inorg. Chem.*, **2007**, *46*, 299-308. c) P. Kar, M. Yoshida, Y. Shigeta, A. Usui, A. Kobayashi, T. Minamidate, N. Matsunaga, and M. Kato, *Angew. Chem. Int. Ed.*, **2017**, *56*, 2345-2349.

(18) Y.-J. Li, Z.-Y. Deng, X.-F. Xu, H.-B. Wu, Z.-X. Cao and Q.-M. Wang, *Chem. Commun.,* **2011**, *47*, 9179-9181.

(19) a) G. M. Espallargas, L. Brammer, J. van de Streek, K. Shankland, A. J. Florence, and H. Adams, *J. Am. Chem. Soc.*, **2006**, *128*, 9584-9585. b) A. Cingolani, S. Galli, N. Masciocchi, L. Pandolfo, C. Pettinari, and A. Sironi, *J. Am. Chem. Soc.,* **2005**, *127*, 6144-6145.

(20) B. Li, R.-J. Wei, J. Tao, R.-B. Huang, L.-S. Zheng and Z. Zheng, *J. Am. Chem. Soc.,* **2010**, *132*, 1558–1566.

(21) a) K. Yamada, S. Yagishita, H. Tanaka, K. Tohyama, K. Adachi, S. Kaizaki, H. Kumagai, K. Inoue, R. Kitaura, H.-C. Chang, S. Kitagawa and S. Kawata, *Chem. Eur. J.*, **2004**, *10*, 2647-2660. b) D. Braga, L. Maini, P. P. Mazzeo and B. Ventura, *Chem. Eur. J.*, **2010**, *16*, 1553-1559. c) Z.-Z. Lu, R. Zhang, Y.-Z. Li, Z.-J. Guo and H.-G. Zheng, *J. Am. Chem. Soc.*, **2011**, *133*, 4172-4174. d) N.-N. Yang, W. Sun, F.-G. Xi, Q. Sui, L.-J. Chen and E.-Q. Gao, *Chem. Commun.*, **2017**, *53*, 1747-1750.

(22) a) J.-R. Li, R. J. K. and H.-C. Zhou, *Chem. Soc. Rev.*, **2009**, *38*, 1477-1504. b) B. Chen, S. Xiang and G. Qian, *Acc. Chem. Res.*, **2010**, *43*, 1115-1124.

(23) A. Kobayashi, H. Hara, S. Noro and M. Kato, *Dalton Trans.*, **2010**, *39*, 3400–3406.

(24) M. Kato, S. Kishi, Y. Wakamatsu, Y. Sugi, Y. Osamura, T. Koshiyama, M. Hasegawa, *Chem. Lett.,* 2005, 34, 1368-1369.

(25)T. Yonemura, Master Thesis, Hokkaido University, March, 2010.

Chapter 2

Shape-Memory Platinum(II) Complexes: Intelligent Vapor-History Sensor with ON–OFF Switching Function

2-1 Introduction

Although a lot of examples showing the Type I vapochromism have been reported so far[1], there is no report about the controllability of the Type I vapochromism probably due to the difficulty in the control of both the crystal structure and vapor adsorption behavior. Especially, most of the Type I vapochromic materials are basically classified to molecular crystals constructed by weak intermolecular interaction[2], which make it more difficult to control of crystal structure. To overcome this difficulty, the unique Type I vapochromic complex, $[Pt(CN)_2(H_2dcbpy)]$ (**1** ; H_2dcbpy = 4,4'-dicarboxy-2,2'-bipyridine) was selected as the standard reference, because this complex was reported to form a porous crystal structure supported by intermolecular hydrogen-bonding and Pt-Pt interactions.[2] The hydrogen-bond-supported porous structure may enable us not only to control systematically the pore size, but also to retain the porous structure. If the pore size could be reduced, the adsorption of large vapor molecule would be prohibited. As the result, more vapor selective vapochromic response for the small vapor could be expected. Since the porous structure of **1** is basically constructed by hydrogen-bonds between the carboxylic acid groups of bipyridine ligand and cyanide ligands, chemical modifications on the bipyridine moiety except for 4,4'- position will not be affected to the porous structure of **1**. Therefore, the phenanthroline analogue complex, $[Pt(CN)_2H_2dcphen]$ (**2** ; $H_2dcphen$ = 4,7-dicarboxy-1,10-phenanthroline) was synthesized. This complex has two carboxylic acids and two cyanide ligands at the same positions of **1** (Scheme 2-1). X-ray diffraction and luminescence measurements were conducted to elucidate vapor selectivity. Moreover, temperature dependences of the crystal structures and luminescence properties of **1** and **2** were also investigated in detail to examine the π-extension effect in the ligand. In this research process, both complexes were found to exhibit a unique "molecular-scale shape-memory" vapochromic behavior. To discuss the detail, vapor adsorption isotherm measurements was also conducted.

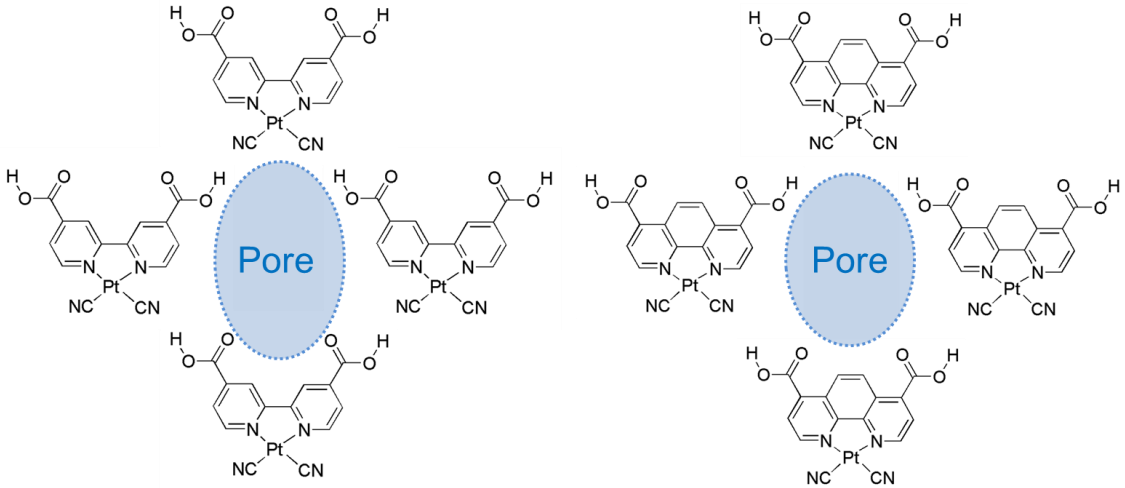

Complex 1
$[Pt(CN)_2(H_2dcbpy)]$

Complex 2
$[Pt(CN)_2(H_2dcphen)]$

Scheme 2-1. Molecular structures of complexes **1** and **2**.

2-2 Experimental section

2-2-1 Materials, synthesis and sample preparation

General procedures

All commercially available starting materials were used without purification. The starting material $Pt(CN)_2$, the amorphous purple form of the bipyridyl complex ($[Pt(CN)_2(H_2dcbpy)]$ (abbreviated as **1P**)), and the red crystalline solid of $[Pt(CN)_2(H_2dcbpy)]\cdot 3H_2O$ (**2R⊃water**) were prepared according to previously published methods.[2] H_2dcphen was synthesized from 4,7-diformyl- 1,10-phenanthroline,[3] and the final oxidation step was conducted according to the synthetic procedure of 2,2':6',2''-terpyridine-4'-carboxylic acid by using $AgNO_3$.[4] ^1H NMR spectra of the samples were measured on a JEOL EX-270 NMR spectrometer at room temperature. Elemental analysis was conducted at the Analysis Center at Hokkaido University.

Amorphous form of $[Pt(CN)_2(H_2dcphen)]$ (=2P)

The yellowish green $Pt(CN)_2$ powder (273 mg, 1.1 mmol) was first suspended in aqueous NH_3 (25 mL) followed by addition of the white H_2dcphen powder (134 mg, 0.5 mmol). The reaction mixture was refluxed at 110°C for one day. After cooling to room temperature, aqueous NH_3 (30 mL) was added to the reaction mixture, which was then refluxed for an additional day. After cooling to room temperature, the resultant yellowish green suspension was collected by filtration. Dilute aqueous HCl (5 mL) was added to the obtained yellow filtrate to promote precipitation of a purple solid, which was collected by centrifugation. The purple solid was suspended in 3% aqueous HCl (200 mL), and the mixture was heated to 100°C for 10 min. The insoluble precipitates were immediately collected though filtration and dried in vacuum to give the desired product in the amorphous purple form (**2P**). Yield: 139 mg, 50%. 1H NMR (4% NaOD in D_2O): d=9.08 (d, 2H), 8.36 (s, 2 H), 7.95 ppm (d, 2H); elemental analysis calcd (%) for $C16H8N4O4Pt\cdot 2H_2O$: C 35.85, H 2.19, N 10.16; found: C 35.93, H 2.04, N 10.45.

Red crystalline solid of $[Pt(CN)_2(H_2dcphen)]\cdot 3H_2O$ (2R-water)

The purple amorphous solid **2P** (10.6 mg, 0.02 mmol) was dissolved in MeOH (1 mL) containing MeOLi/MeOH (120 mL, 10% solution). H_2O (1.3 mL) was then added to this solution. Diffusion of CH_3COOH vapor into the MeOH/water solution gave red crystals of **2R-water** that were suitable for X-ray diffraction analysis.

Preparation of vapor-exposed samples.

The small amount of the sample (ca. 2 mg) was added to a small glass vial and the vial was placed in a larger, capped, glass vial with a small amount of liquid (ca. 1 mL) as the vapor source. The glass vial was left in a temperature-controlled incubator at 303 K for several days.

2-2-2 Physical measurements.

Powder X-ray diffraction: Powder X-ray diffraction was conducted with either a Rigaku SPD diffractometer at beamline BL-8B at the Photon Factory, KEK, Japan or a Bruker D8 Advance diffractometer equipped with a graphite monochromator using CuKa radiation and a one-dimensional LinxEye detector. The wavelength of the synchrotron X-rays was 1.5385(1) Å.

Luminescence properties: The luminescence spectra of the complexes were measured with a JASCO FP-6600 spectrofluorometer at room temperature. The typical slit widths of the excitation and emission light were 5 and 6 nm, respectively. Temperature-dependent luminescence spectra were measured with a Hamamatsu multichannel photodetector (PMA-11) and a nitrogen laser for the 337 nm excitation. A liquid nitrogen cryostat (Optistat-DN optical Dewar and ITC-503 temperature controller, Oxford Instruments) was used for temperature control. The emission lifetime were measured by using a Quantaurus-Tau C11367 (Hamamatsu Photonics K. K.) excited by a UV LED light source (λex = 405 nm). Emission quantum yields were measured on a Hamamatsu C9920−02 absolute photoluminescence quantum yield measurement system equipped with an integrating sphere apparatus and a 150 W continuous wave xenon light source.

Vapor-adsorption isotherms: Vapor-adsorption isotherms of the complexes were measured using BELSORP-max vapor adsorption isotherm measurement equipment at 298 K.

Single-crystal X-ray diffraction measurements: All the measurements of **2R⊃water** were conducted with a Rigaku AFC-11 diffractometer with a Mercury CCD area detector at beamline PF-AR NW2A at the Photon Factory, KEK, Japan. The wavelength of the synchrotron X-rays was 0.6890(1) Å . Temperature-dependent measurements of **1R⊃water** were conducted with a Rigaku Mercury CCD diffractometer with monochromated MoKa radiation (λ= 0.71069 Å) and a sealed X-ray tube generator. All single crystals were mounted on a MicroMount coated with paraffin oil. The crystal was then cooled by using an N_2 flowtype temperature controller.
The diffraction data were collected and processed with Crystal-Clear software.[5] The structures were solved with the direct method by using SIR-2004.[6] Structural refinements were conducted by the full-matrix least-squares method with SHELXL-97.[7] Nonhydrogen atoms were refined anisotropically, and all hydrogen atoms were refined with the riding model. All calculations were conducted with the Crystal Structure crystallographic software package.

2-3 Result and discussion

2-3-1 Crystal structure

Single crystal of **2** was successfully synthesized in the trihydrated form by CH_3COOH vapor diffusion into a basic aqueous solution of the amorphous-like purple solid, **2P**. Figure 2-1 shows the crystal structure of **2R⊃water** compared with **1R⊃water**, and selected bond lengths and angles at various temperature are listed in **Table 2-1 and 2-2**. As expected from the similarity of the molecular structures of **1** and **2**, the phenanthroline complex, **2R⊃water**, was found to be isomorphous to the bipyridine complex, 2R-water. The central Pt(II) ion features typical square-planar coordination geometry with coordination to two nitrogen atoms of H_2dcphen and two carbon atoms from the cyanide ligands. All the atoms of this complex are located in the same ab plane. The bond lengths around the Pt(II) ion, that is, Pt-C (1.960(5) Å) and Pt-N (2.041(4) Å), are almost equal to those in **1R⊃water**. The two C-O bond lengths of the carboxyl group are very different (1.304(9) and 1.201(8) Å), indicating that the O(2) atom with the longer C-O bond is protonated. Judging from the O(2)-H···N(3) distance (2.652(7) Å) between the protonated carboxyl group and cyanide ligand of the adjacent molecule, relatively tight hydrogen bonds formed between these functional groups. As a result, the two-dimensional hydrogen-bonded network is constructed in the ab plane. On the other hand, the fully planar Pt(II) complex molecules are stacked along the c axis in an antiparallel orientation to cancel out the dipole moment of each molecule, as shown in Figure 1 (a). The intermolecular Pt・・・Pt distance (3.2355(3) Å) is slightly longer than that of **1R⊃water** (3.2161(6) Å), but remain significantly shorter than twice the van der Waals radius of the platinum atom (3.50 Å), indicating that the metallophilic interaction is effective in this one-dimensional stacked structure. Notably, the Pt···Pt···Pt stacking angle (166.73(1) Å) is about 5.16° smaller than that of **1R⊃water** (171.89(2) °), suggesting that the π–π stacking interactions in **2R⊃water** are more effective than those in **1R⊃water**, resulting in the formation of a more twisted one-dimensional zig-zag chain structure. As shown in Figure 1(b), one-dimensional large porous channels forms along the c axis, and the pore size is estimated to be about 6.4×6.8 Å, which is smaller than that of **1R⊃water** (6.1×8.8 Å). Single-crystal X-ray structural analysis also revealed that this crystal contains at least three hydrated water molecules per Pt(II)-complex molecule in the pores. By using the SQUEEZE program, the void fraction of **2R** was estimated to be 35.2% in the unit cell, which is also smaller than that of **1R** (39.5%) (note: the hydrated water molecules in the pore were excluded in these calculations); this is due to the larger molecular volume of the H_2dcphen ligand than that of H_2dcbpy.

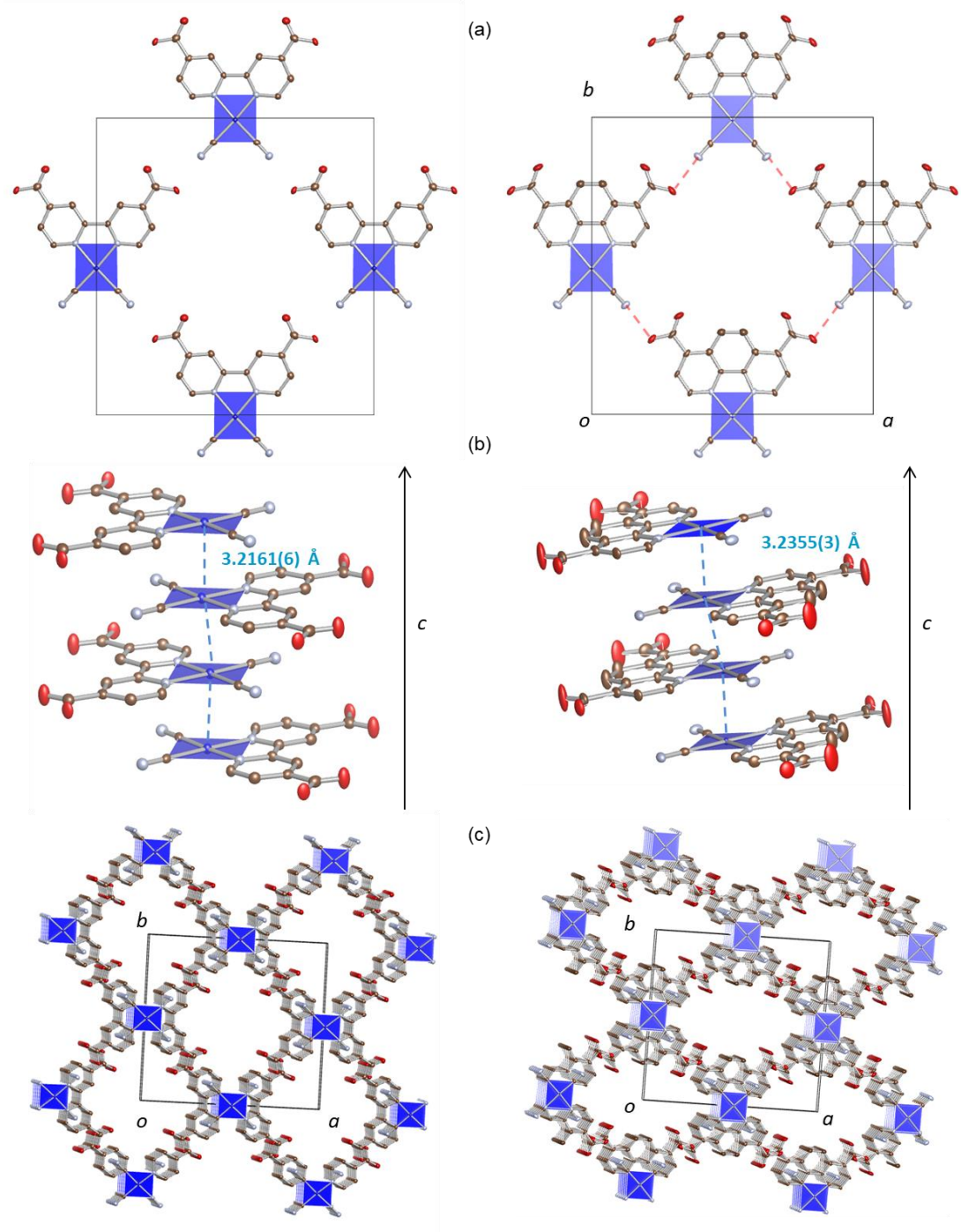

Figure 2-1. Crystal structure of **1R⊃water**(left) and **2R⊃water**(right). a)two-dimensional hydrogen bonding in ab plane. b)one-dimensional Pt-Pt stacking structure along the c axis. c) porous structure. Hydrogen atoms and solvent molecules were omitted for clarity.

Table 2-1. Crystal parameters and refinement data of red form **1R⊃water** and **2R⊃water**.

Complex	**1R⊃water**					
T / K	100	125	150	175	200	225
Formula	$PtC_{14}H_8N_4O_4 \cdot 3H_2O$	$PtC_{14}H_8N_4O_4 \cdot 3H_2O$	$PtC_{14}H_8N_4O_4 \cdot 3H_2O$	$PtC_{14}H_8N_4O_4 \cdot 3H_2O$	$PtC_{14}H_8N_4O_4 \cdot 3H_2O$	$PtC_{14}H_8N_4O_4 \cdot 3H_2O$
Formula weight	545.37	545.37	545.37	545.37	545.37	545.37
Crystal system	Orthorhombic	Orthorhombic	Orthorhombic	Orthorhombic	Orthorhombic	Orthorhombic
Space group	*Cmcm*	*Cmcm*	*Cmcm*	*Cmcm*	*Cmcm*	*Cmcm*
a / Å	17.323(4)	17.329(4)	17.326(4)	17.320(4)	17.353(6)	17.332(3)
b / Å	18.589(4)	18.592(4)	18.590(4)	18.601(4)	18.608(6)	18.610(3)
c / Å	6.4160(12)	6.4288(12)	6.4408(12)	6.4611(13)	6.494(2)	6.5127(11)
α / deg.	90	90	90	90	90	90
β / deg.	90	90	90	90	90	90
γ / deg.	90	90	90	90	90	90
V / Å^3	2066.1(8)	2071.2(8)	2074.5(8)	2081.6(8)	2096.9(12)	2100.7(6)
Z	4	4	4	4	4	4
D_{cal}/ g·cm^{-3}	1.753	1.749	1.746	1.74	1.727	1.731
Reflections collected	11133	11164	11182	11215	11318	11362
Unique reflections	1332	1335	1335	1339	1344	1350
GOF	1.223	1.226	1.261	1.240	1.229	1.243
R_{int}	0.0742	0.0748	0.0769	0.0752	0.0817	0.0830
R (I > 2.00σ(I))	0.0387	0.0394	0.0414	0.0419	0.0412	0.0401
R_W [a]	0.1025	0.0985	0.1087	0.1079	0.1062	0.1037
Complex	**2R⊃water**					
T / K	100	125	150	175	200	225
Formula	$PtC_{16}H_8N_4O_4 \cdot 3H_2O$	$PtC_{16}H_8N_4O_4 \cdot 3H_2O$	$PtC_{16}H_8N_4O_4 \cdot 3H_2O$	$PtC_{16}H_8N_4O_4 \cdot 3H_2O$	$PtC_{16}H_8N_4O_4 \cdot 3H_2O$	$PtC_{16}H_8N_4O_4 \cdot 3H_2O$
Formula weight	569.39	569.39	569.39	569.39	569.39	569.39
Crystal system	Orthorhombic	Orthorhombic	Orthorhombic	Orthorhombic	Orthorhombic	Orthorhombic
Space group	*Cmcm*	*Cmcm*	*Cmcm*	*Cmcm*	*Cmcm*	*Cmcm*
a / Å	17.5971(18)	17.598(2)	17.595(3)	17.596(3)	17.587(4)	17.595(5)
b / Å	18.2775(19)	18.280(3)	18.289(3)	18.276(4)	18.288(5)	18.279(5)
c / Å	6.4277(7)	6.4427(7)	6.4580(8)	6.4733(11)	6.4903(15)	6.5122(17)
α / deg.	90	90	90	90	90	90
β / deg.	90	90	90	90	90	90
γ / deg.	90	90	90	90	90	90
V / Å^3	2067.3(4)	2072.6(5)	2078.2(6)	2081.7(7)	2087.5(9)	2094.4(10)
Z	4	4	4	4	4	4
D_{cal}/ g·cm^{-3}	1.829	1.825	1.820	1.817	1.812	1.806
Reflections collected	11666	11752	12260	12114	12292	12269
Unique reflections	1434	1436	1440	1442	1445	1453
GOF	1.203	1.127	1.090	1.109	1.082	1.139
R_{int}	0.0635	0.0472	0.0518	0.0604	0.0828	0.0881
R (I > 2.00σ(I))	0.0261	0.0404	0.0407	0.0500	0.0326	0.0359
R_W [a]	0.0593	0.0875	0.0853	0.1402	0.0805	0.0871

[a] $R_W = [\Sigma(w(F_o^2 - F_c^2)^2)/\Sigma w(F_o^2)^2]^{1/2}$.

Table 2-2. Selected bond distances and angles of **1R⊃water** compared with **2R⊃water**.

Complex	**1R⊃water**					
T / K	100	125	150	175	200	225
Pt1-N1	2.046(7)	2.051(7)	2.051(7)	2.052(7)	2.049(7)	2.054(7)
Pt1-C7	1.952(8)	1.955(8)	1.953(9)	1.950(10)	1.959(9)	1.951(10)
O1-H···N3	2.650(11)	2.660(11)	2.660(11)	2.662(11)	2.664(11)	2.680(11)
Pt1···Pt1	3.2161(6)	3.2224(6)	3.2284(6)	3.2387(6)	3.2550(10)	3.2642(6)
diimine-CN	3.208	3.214	3.220	3.231	3.247	3.256
Pt1···Pt1···Pt1	171.886(16)	171.940(16)	171.917(16)	171.845(16)	171.962(16)	172.062(16)
Complex	**2R⊃water**					
T / K	100	125	150	175	200	225
Pt1-N1	2.041(4)	2.047(7)	2.045(7)	2.029(11)	2.047(5)	2.050(5)
Pt1-C7	1.960(5)	1.963(6)	1.960(6)	1.941(13)	1.962(5)	1.957(6)
O1-H···N3	2.652(7)	2.665(10)	2.669(9)	2.694(16)	2.665(8)	2.660(10)
Pt1···Pt1	3.2355(3)	3.2433(4)	3.2508(4)	3.2583(6)	3.2668(7)	3.2768(8)
diimine-CN	3.214	3.221	3.229	3.237	3.245	3.256
Pt1···Pt1···Pt1	166.73(1)	166.655(15)	166.735(15)	166.79(2)	166.80(1)	167.108(14)

2-3-2 Multichromism

Kato and co-workers have previously reported about the vapor-induced color/luminescence change of **1P**. In this work, the vapochromic behavior of 2P was examined because of the isomorphous structures of **1R⊃water** and **2R⊃water**. Figure 2-2 shows changes in the emission spectrum of **2P** under exposure to several different vapors for five days in comparison with that of the red crystalline **2R⊃water**. The observed emission maxima for both complexes are summarized in Table 2-3. The initial purple solid, **2P**, shows weak luminescence at 733 nm, which is 11 nm shorter than that of bipyridine complex **1P**. Interestingly, bright red luminescence centered at around 630 nm was observed after exposure of **2P** to MeOH, EtOH, 2-PrOH, and 2-BuOH vapors for five days at 303 K, as shown in Figure 2 (a). The emission maxima for these vapor-exposed samples are very close to that observed for the red crystalline **2R⊃water**, suggesting that the emission can be attributed to the ^{3}MMLCT (triplet metal-metal to ligand charge transfer) transition state generated by effective Pt・・・Pt interactions. In contrast, no change was observed under exposure of **2P** to nonpolar organic vapors, such as n-hexane (Figure 2-3). Very similar luminescence changes under exposure to alcoholic vapors were also observed for bipyridine complex **1P**, as reported previously.[] A remarkable difference between these two complexes was observed in *t*-BuOH vapor: Although the emission maximum of **1P** changed to 638 nm after exposure

to *t*-BuOH vapor, the spectrum of 1P did not change at all. Considering that both complexes show bright red emission centered at around 640 nm upon exposure to 2-BuOH, both

the bulky *t*-Bu group of *t*-BuOH vapor and the smaller pore size of **2R** may be plausible explanations for why **2P** did not change upon exposure to *t*-BuOH vapor.

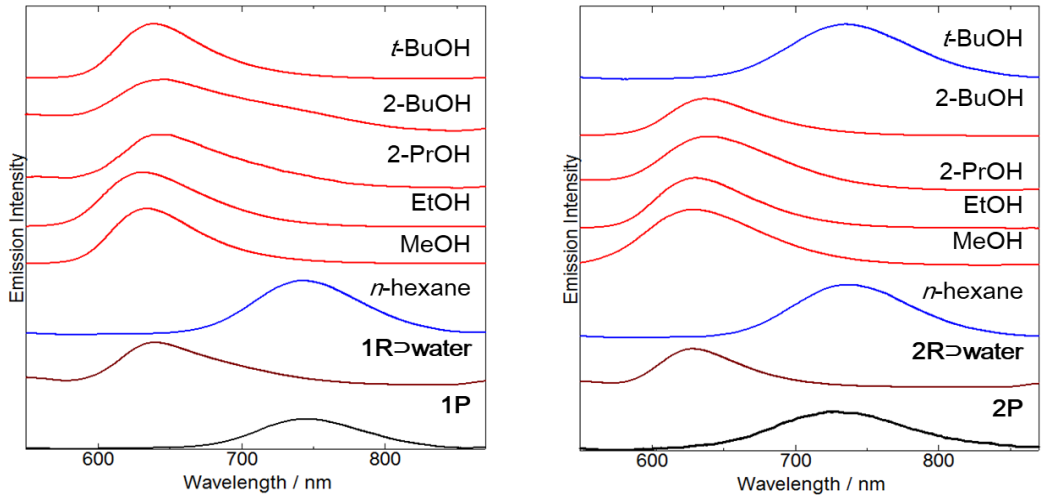

Figure 2-2. Changes of the luminescence spectra of **1P** (left) and **2P** (right) after exposure to various solvent vapors at 30°C for five days (λ_{ex}=400 nm). Spectra of the red crystalline **1R⊃water** and **2R⊃water** are included for comparison.

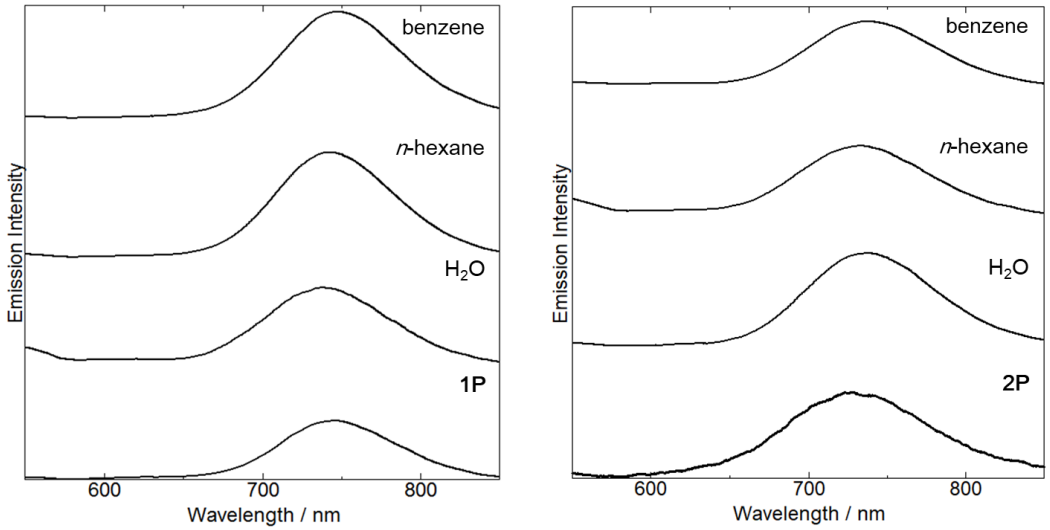

Figure 2-3. Changes of the luminescence spectra of (a) **1P** and (b) **2P** after exposure to H_2O and non-polar solvent vapors at 30°C for five days (λ_{ex}=400 nm).

Table 2-3. Emission maxima of **1P** and **2P** (λ_{ex}= 400 nm) after exposure to various solvent vapors.

1P		**2P**	
state or vapor source	λ_{em} (nm)	state or vapor source	λ_{em} (nm)
1P	744	2P	733
1R	640	2R	628
n -hexane	745	*n* -hexane	736
MeOH	633	MeOH	627
EtOH	632	EtOH	625
2-PrOH	643	2-PrOH	638
2-BuOH	648	2-BuOH	638
t -BuOH	638	*t* -BuOH	734

To elucidate the origins of the luminescence changes of **2P** in the presence of alcoholic vapors, powder X-ray diffraction (PXRD) patterns were measured for vapor-exposed **1** and **2**. As shown in Figure 2-4, **1P** and **2P** showed very broad patterns, indicating that these purple solids are almost amorphous. After exposing these amorphous-like solids to alcohol vapor, dramatic changes were observed in the luminescence spectra. The observed PXRD patterns of **1** and **2** exposed to MeOH, EtOH, 2-PrOH, and 2-BuOH were almost identical to the simulated patterns calculated from the crystal structures of **1R⊃water** and **2R⊃water**, respectively. These results indicate that a vapor-induced amorphous-crystalline transformation occurred in the presence of these alcoholic vapors to form vapor-adsorbed porous phases of **1R⊃vapor** and **2R⊃vapor** with effective Pt ⋯ Pt interactions. TG-DTA analysis and vapor adsorption isotherm measurements revealed that these two Pt(II) complexes adsorbed the alcoholic vapors (see below and Figure 2-5). As a result, the luminescence maxima of vapor-adsorbed **1R⊃vapor** and **2R⊃vapor** are very similar to those of **1R⊃water** and **2R⊃water**, respectively (Figure 2-2). The PXRD patterns upon exposure to *t*-BuOH vapor also show a very clear difference between the behavior of **1P** and **2P**. The PXRD pattern of the phenanthroline complex **2P** only showed a negligible change upon exposure to *t*-BuOH vapor, whereas that of the bipyridine complex **1P** after exposure is almost identical to the simulated pattern of **1R⊃water**. This difference is attributed to the differences in the pore sizes. The pores of the bipyridine complex **1R** (*ca.* 6.1×8.8 $Å^2$) are larger than those of the phenanthroline complex **2R** (*ca.* 6.4×6.8 $Å^2$); this enables **1R** to adsorb *t*-BuOH vapor, resulting in large changes of both the emission and PXRD spectra in the presence of *t*-BuOH vapor. On the other hand, the PXRD patterns of both **1P** and **2P** were not affected by exposure to nonpolar vapor and water vapor (Figure 2-6). The nonpolar vapors were not adsorbed into the pores because the porous structures of these complexes consist of two-dimensional hydrogen-bonding networks between hydrophilic carboxyl and cyanide groups. Although water molecules have large dipole moments, the structural transformation from **2P** to **2R⊃vapor** was not observed; this implies that a certain molecular volume of the vapors is required to trigger the transformation. The transformation was hardly observed under exposure to 1,1,1-trichloroethane vapor, which has almost the same molecular shape and volume as *t*-BuOH (Figure 2-7). Hence, the hydrogen donating ability of the alcohols is important to trigger the transformation.

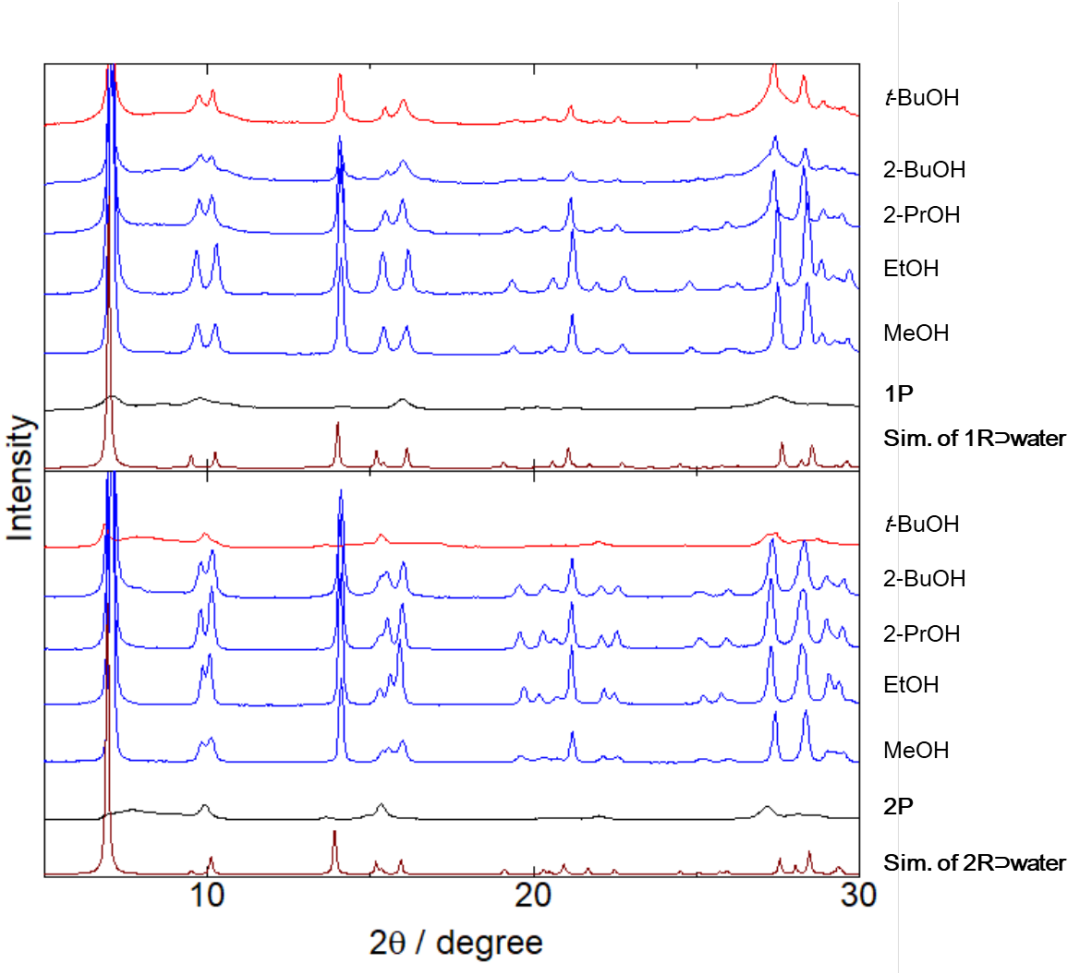

Figure 2-4. Powder X-ray diffraction patterns (λ=1.5385 Å) of the amorphous purple powders of **1P** (top) and **2P** (bottom) upon exposure to several alcoholic vapors. The bottom lines show the simulated pattern calculated from the crystal structure at 100 K. The exposure time for each vapor was five days at 30ºC.

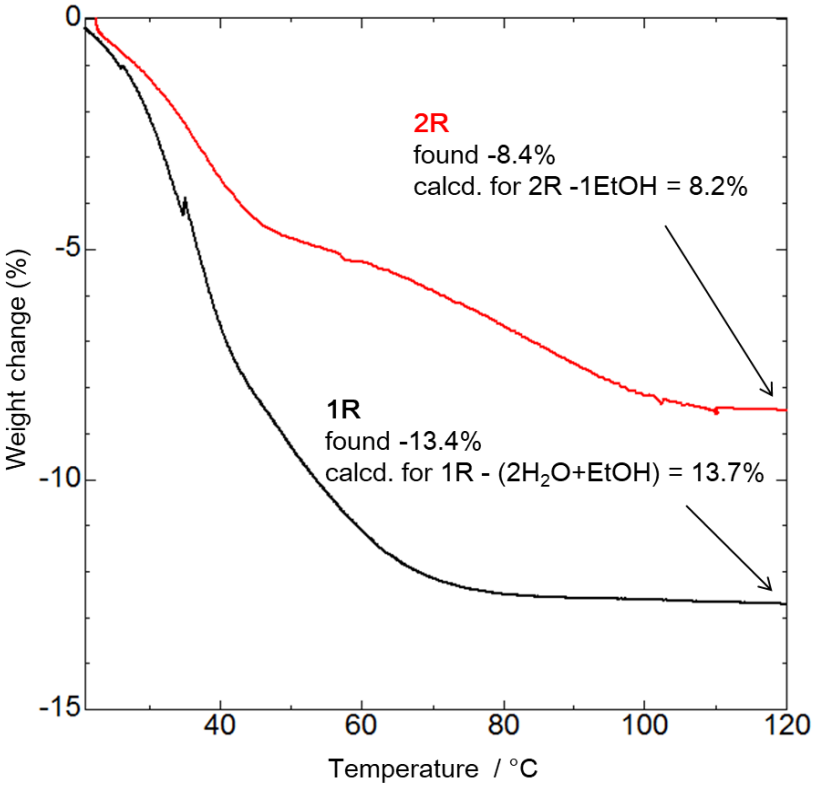

Figure 2-5. Thermogravimetric analysis for **1R⊃EtOH** (black) and **2R⊃EtOH** (red).

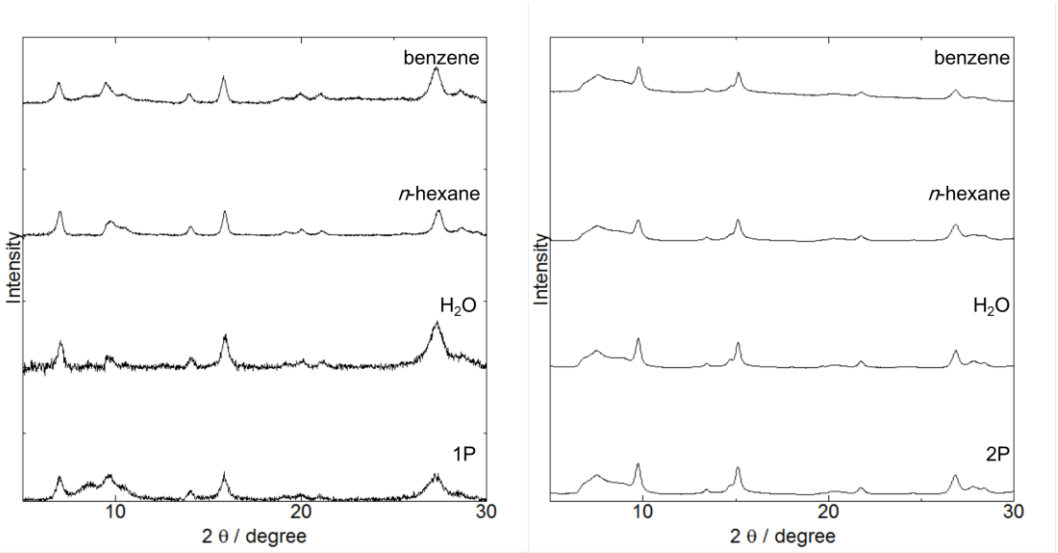

Figure 2-6. Changes in PXRD patterns of **1P**(left) and **2P**(right) after exposing it to water, *n*-hexane or benzene vapor.

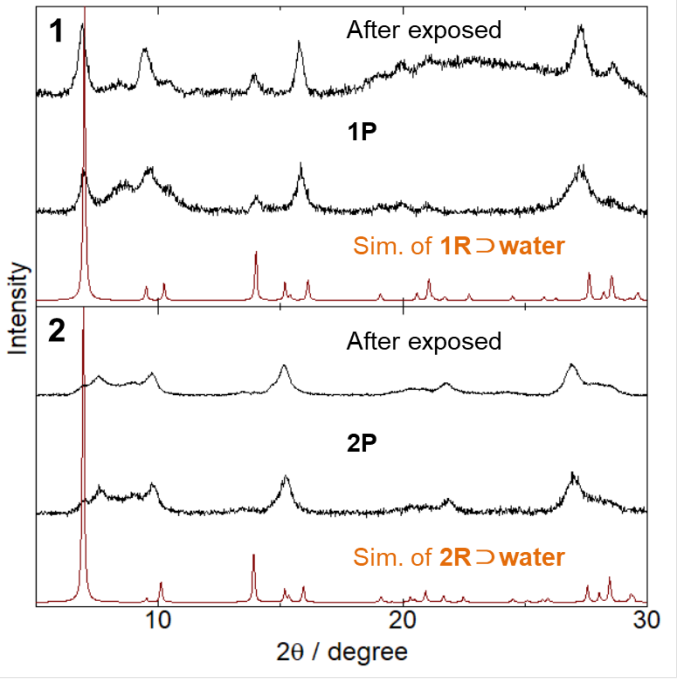

Figure 2-7. PXRD patterns of Powder X-ray diffraction patterns (λ = 1.54 Å) of amorphous purple powders of **1P** and **2P** upon exposure to 1,1,1-trichloroethane vapor for 5 days at 30°C.

Next, desorption process of the adsorbed alcoholic vapors were examined desorption . As shown in Figure 2-8 (a), **2R⊃EtOH** exhibited red luminescence at 630 nm. After desorption of EtOH by heating at 383 K (as confirmed by TG analysis, Figure 2-5), the luminescence maximum shifted to 653 nm, which is still remarkably shorter than that of the initial purple solid, **2P**. The observed PXRD pattern after desorption of EtOH by heating is still very similar to that of the EtOH-adsorbed complex and the simulated pattern of **2R⊃water**, indicating that the porous structure of **2R** is retained even after removal of EtOH to form open-channel structures in **2R⊃open**. The diffraction peak observed at about 27º, which was indexed to (002) and corresponds to the direction of the intermolecular Pt···Pt interactions, was negligibly shifted by removal of EtOH (Figure 2-9). On the other hand, the lattice constant refinements and lattice mismatch calculation for these PXRD patterns suggested that removal of EtOH significantly affected the *ab* plane rather than the *c* axis (Table 2-4, 2-5). Lattice constants for *a* and *b* axis hardly affected by temperature (see Figure 2-18), this change should be induced by the adsorbed EtOH molecules. Thus, the intermolecular Pt···Pt interactions could be strengthened by EtOH removal probably because of slipping of the planar [$Pt(CN)_2(H_2dcphen)$] molecules in the ab plane to form more linear Pt–Pt stacking structures, resulting in a red shift of the ^{3}MMLCT emission. Therefore, the porous structure of **2R** can be formed by adsorption of alcoholic vapors into the porous channels to form **2R⊃vapor**, and removal of the guest molecules does not degrade the porous structure of **2R** to give the open framework of **2R⊃open**. However, it has a significant impact on the intermolecular Pt···Pt interactions via slipping to linearize the Pt–Pt–Pt stacking angle. To elucidate the effect of the guest EtOH molecule for photophysical properties, emission quantum yield and lifetime measurements were conducted and summarized in Table 2-6. Although solvent molecules having hydroxy group often affects these parameters because of its vibrational deactivation process, almost same quantum yield, lifetime, k_r and k_{nr} values were obtained. This result may be coming from the conflict of vibrational deactivation and energy gap law. Interestingly, the EtOH-desorbed **2R⊃open** showed dramatic color and luminescence changes upon manual grinding in a mortar, as shown in Figure 2-8 (a): The color of the sample changed from red to purple and the luminescence band of the ground sample was observed at 724 nm, which is close to that of the initial purple solid, **2P**. In addition, the observed PXRD pattern of the ground sample was very broad. Thus, the EtOH-desorbed **2R⊃open** was transformed to the weakly emissive purple amorphous-like solid **2P** by manual grinding.

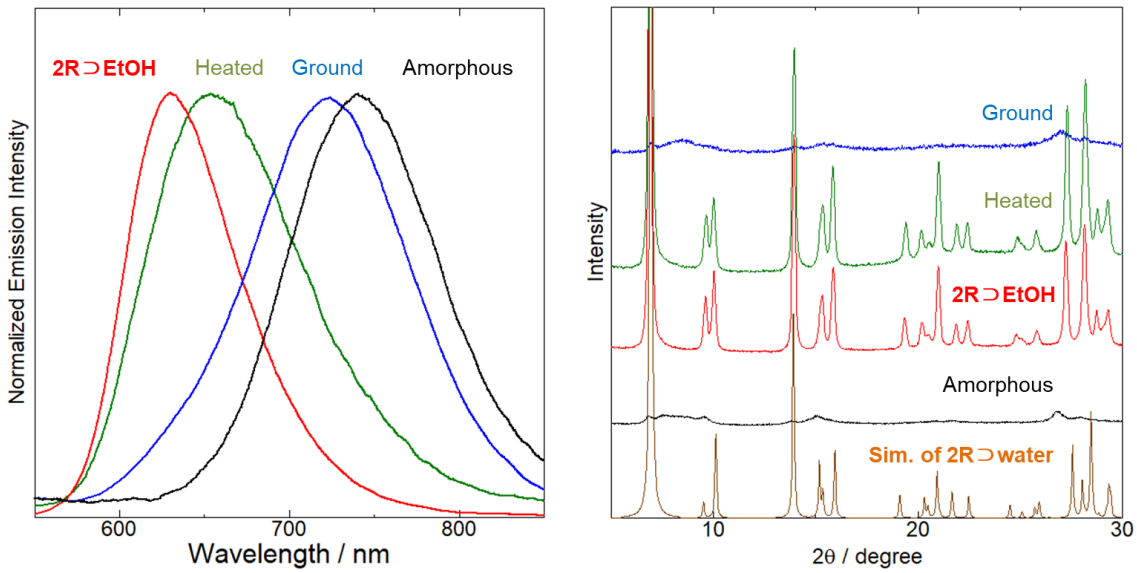

Figure 2-8. Changes in the luminescence spectra (left, λ_{ex}=400 nm) and the powder X-ray diffraction patterns (right, λ=1.5418 Å) of **2R⊃EtOH**, **2R⊃EtOH** after heating, and **2R⊃EtOH** after heating and grinding. The second lines from the bottom in both panels show the emission spectrum and PXRD pattern of **2P**. The bottom pattern in (b) is the simulated pattern calculated from the crystal structure of **2R⊃water**. The arrow in (b) indicates the position of the (002) reflection.

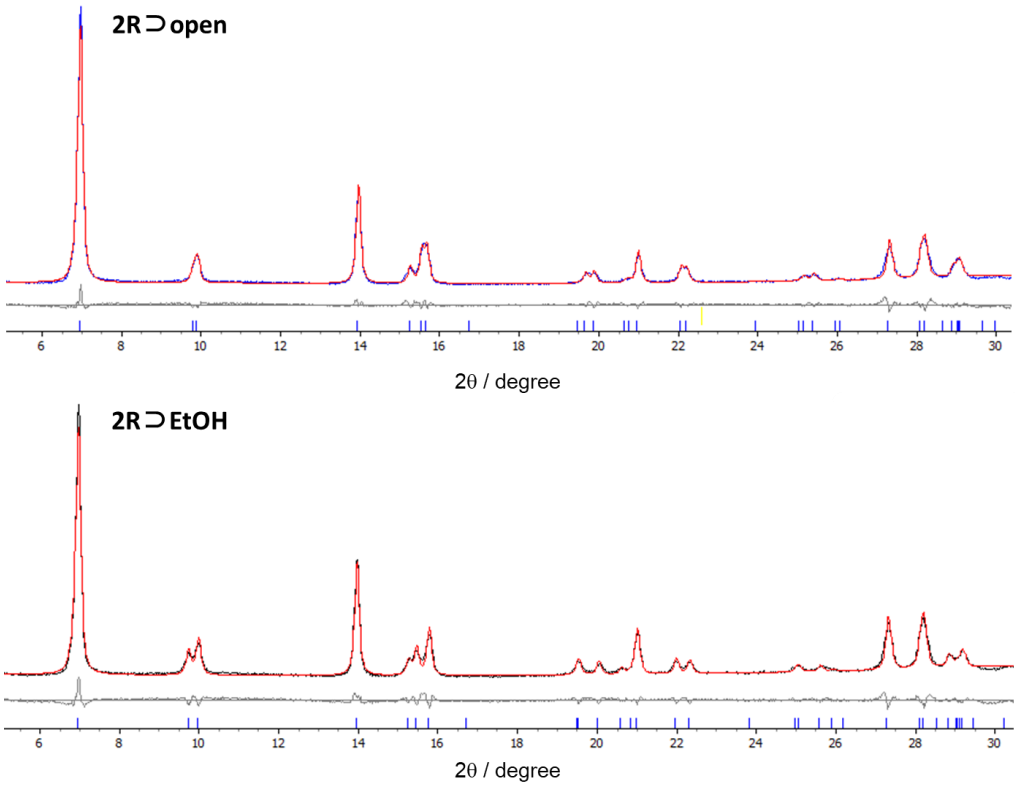

Figure 2-9. Observed PXRD patterns and lattice constant refinement profiles of **2R⊃EtOH**(top) and **2R⊃open** (bottom)**.**

Table 2-4. Lattice constant refinements for PXRD patterns of **2R⊃EtOH** and **2R⊃open** (shown in **Figure 2-9**) by using TOPAS 4 program.[8)]

	2R⊃EtOH	**2R⊃open**
a / Å	17.683(2)	17.819(2)
b / Å	18.133(13)	18.006(2)
c / Å	6.5257(6)	6.5270(6)

Table 2-5. Lattice mismatch calculation results for **2R⊃EtOH** and **2R⊃open** (shown in Figure 2-9) compared with the crystal at 100 K.

	a axis	*b axis*	*c axis*	total
2R⊃EtOH	0.49%	-0.79%	1.52%	1.22%
2R⊃open	1.26%	-1.49%	1.54%	1.32%

Table 2-6. Photophysical parameters for **2R⊃EtOH** and **2R⊃open**.

	quantum yield	Lifetime (μs)	k_r (s^{-1})	k_{nr} (s^{-1})	λ_{em}
2R⊃EtOH	0.05	0.068	7.35×10^5	1.40×10^7	630
2R⊃open	0.04	0.070	5.71×10^5	1.37×10^7	656

2-3-3 “Molecular-scale shape-memory effect” and ON–OFF switching of the vapochromism

To confirm that the vapochromism was derived from vapor adsorption, I measured the vapor adsorption isotherm of **2** upon exposure to EtOH vapor (Figure 2-10). The same sample was used continuously, whereas pretreatments before the measurements varied. The first measurement was performed on purple amorphous **2P** that had been heated in vacuum. Although negligible vapor adsorption was observed at a relative pressure (P/P_0) < 0.4, a large vapor uptake of up to 1.8 molmol^{-1} was observed above P/P_0=0.4. The desorption process was clearly different from the adsorption process: The number of adsorbed EtOH molecules slowly decreased, but still retained 0.9 molmol^{-1} at very low relative pressure ($P/P_0 = 8.6\times10^{-3}$). Considering that **2P** transformed to the red crystalline vapor-adsorbed form, **2R⊃EtOH**, under exposure to EtOH vapor, the sharp increase of EtOH vapor uptake at around P/P_0=0.4 and large hysteresis between the adsorption and desorption processes likely originate from the structural transformation from the nonporous amorphous-like solid, 1P, to the EtOH-adsorbed porous crystalline solid of **2R⊃EtOH**. The EtOH that remains at very low pressure (about 1 mol mol^{-1}) during the desorption process suggests that the adsorbed EtOH molecules were strongly bound in the pore probably by the formation of hydrogen bonds with the carboxyl groups of the porous framework. Next, I measured the second vapor adsorption isotherm by using the same sample as in the first measurement. Before the second cycle, the sample was heated at 120 ºC for one day to completely remove the adsorbed EtOH from the pores to obtain a vapor-free red crystalline **2R⊃open**. Interestingly, the obtained isotherm was significantly different from the first adsorption isotherm, as shown in Figure 2-10: In the second isotherm, a large amount of EtOH adsorbed at a very low relative pressure (*ca.* 0.83 molmol^{-1} at P/P_0=0.1). In contrast, the saturated adsorption amount and desorption behavior were almost the same as those in the first cycle. The sharp increase of vapor uptake at very low pressure is characteristic of microporous materials, and indicates that the EtOH-desorbed **2R⊃open** contained micropores at the beginning of the second measurement. Therefore, the porous structure constructed by EtOH adsorption (i.e., gate-opening behavior) during the first adsorption process could be retained after removal of EtOH by heating during the pretreatment of the second cycle. The purple amorphous form, **2P**, did not convert to the vapor-free porous **2R⊃open** at increasing temperatures in a vacuum (and vice versa; see Figures 2-11 and 2-12). Interestingly, this characteristic feature of the microporous materials observed in the second isotherm completely disappeared during the third cycle during which the sample was heated at 120ºC for one day to remove EtOH and then manually ground in a mortar to regenerate amorphous **2P**, which was heated again in vacuum at 120ºC for one day before the third measurement. The observed isotherm in the third measurement was similar to that of the first one with a large hysteresis

between the adsorption and desorption processes, indicating that the porous form of **2R**, which was constructed in the first EtOH-adsorption cycle and retained in the second cycle, was broken down by manual grinding to the nonporous amorphous **2P** during the pretreatment in the third cycle. Kitagawa and co-workers reported similar behavior on a meso-scale porous coordination polymer (PCP) constructed from Cu^{2+} ions and organic bridging ligands, named as "molecular-scale shape memory effect".[9] The PCP exhibited transformation from original shape to temporary shape upon vapor adsorption. Interestingly, the temporary shape of the down-sized crystal was maintained after gas desorption, and the temporary shape can be recovered by heating. These adsorption measurements in three cycles demonstrate that **2** exhibits the "molecular-scale shape-memory" behavior, that is, this complex can memorize vapor-adsorption history by forming the porous structure, **2R**. The vapor-adsorption history is retained even after removal of the adsorbed vapors, but can be cleared by removal of the vapor followed by manual grinding to form the nonporous amorphous purple form, **2P**. This intelligent vapor-sensing function based on shape-memory behavior was also observed for the bipyridine analogue **1** (see Figure 2-13), suggesting that the lattice stability of the porous structure is supported by a two-dimensional hydrogen-bonded network in the ab plane and a one-dimensional intermolecular metallophilic interaction along the c axis.

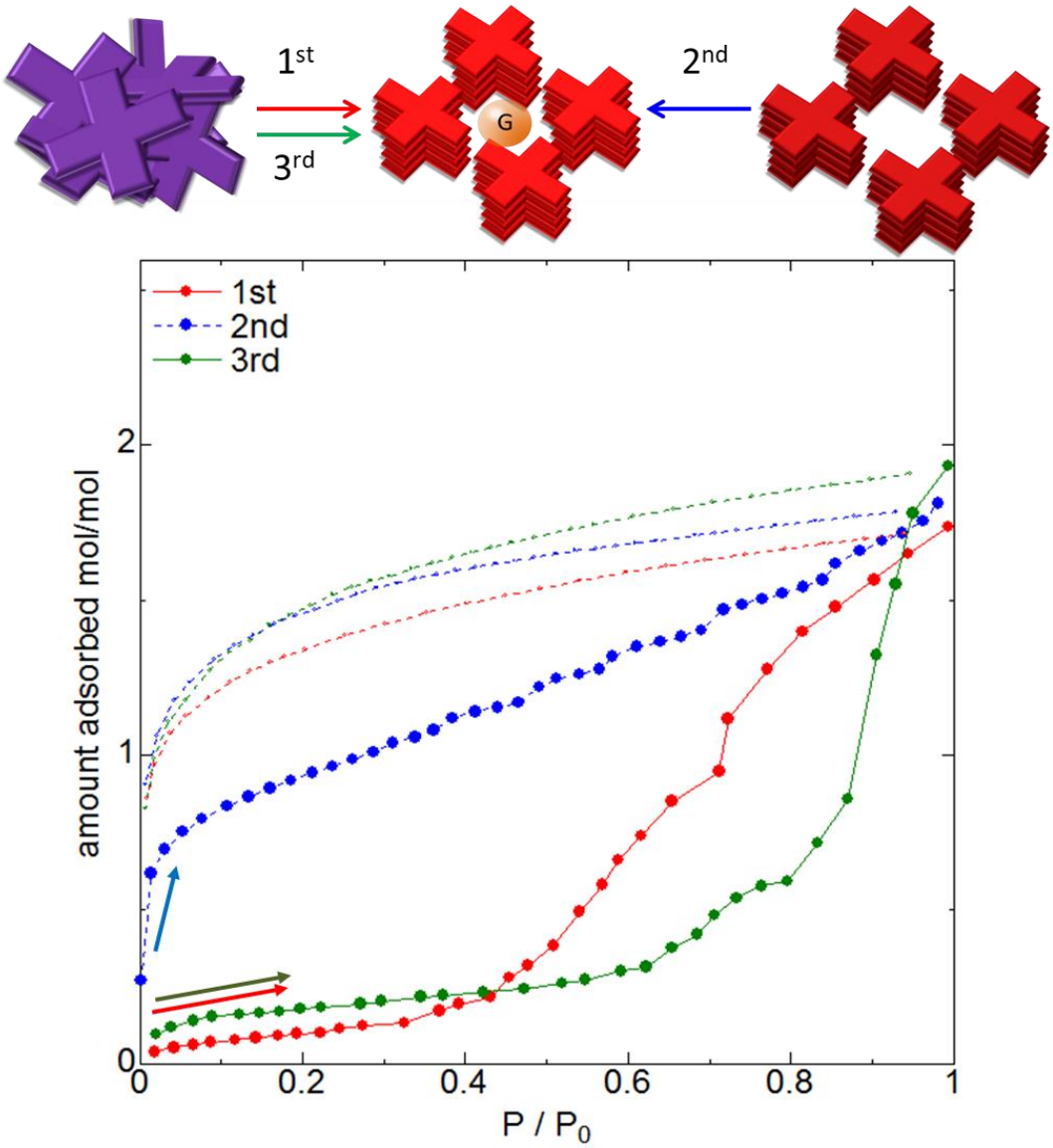

Figure 2-10. EtOH-vapor adsorption isotherms of **2** at 298 K with a schematic illustration of the adsorption processes. The same sample was used in these three measurements with different pretreatments. The amorphous purple form **2P** was used for the first measurement (red). Before the second measurement (blue), the sample was heated in vacuum at 120ºC to obtain the vapor free red crystalline **2R⊃open**. Before the third measurement (green), the sample was heated in vacuum at 120ºC and then manually ground in a mortar at room temperature to generate the amorphous purple form **2P**, which was heated again at 120ºC to remove all water adsorbed during the grinding process. Closed and open symbols show the adsorption and desorption processes, respectively.

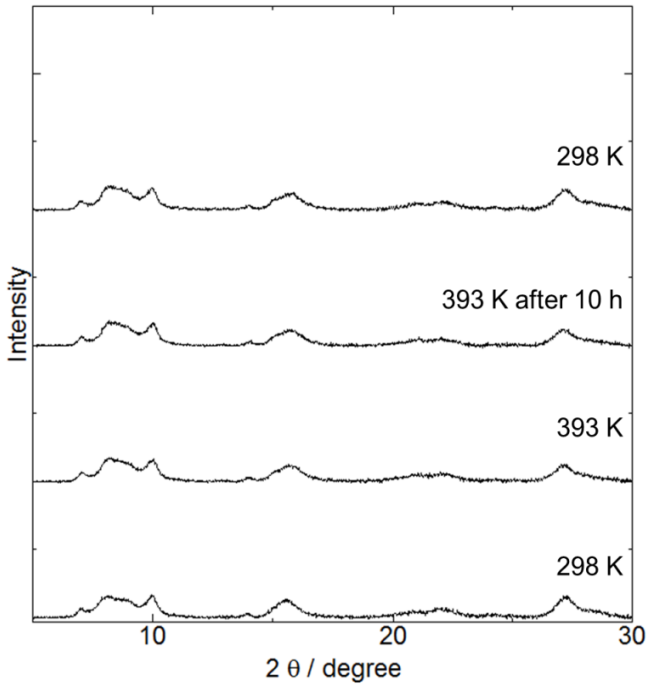

Figure 2-11. Temperature dependence of the PXRD patterns of **2P** under vacuum. The same sample was used for all the measurements.

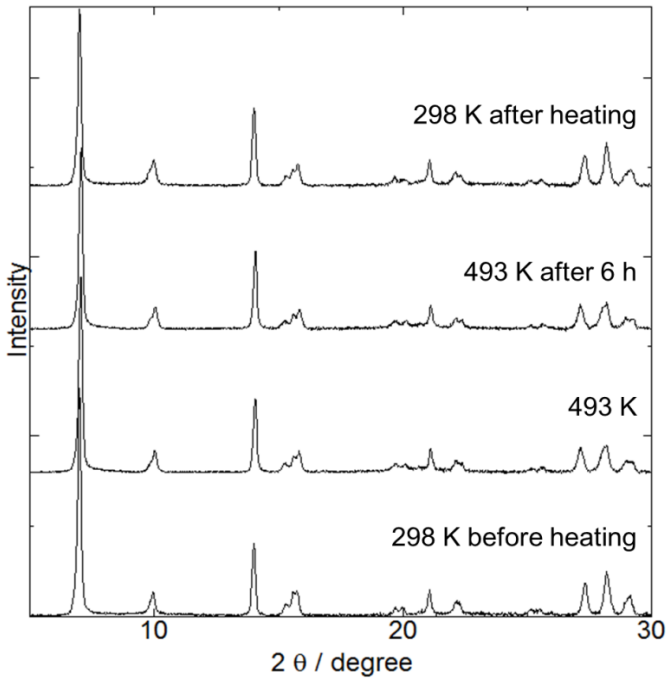

Figure 2-12. Temperature dependence of the PXRD patterns of **2R⊃open** with heating in vacuum. The same sample was used for all measurements.

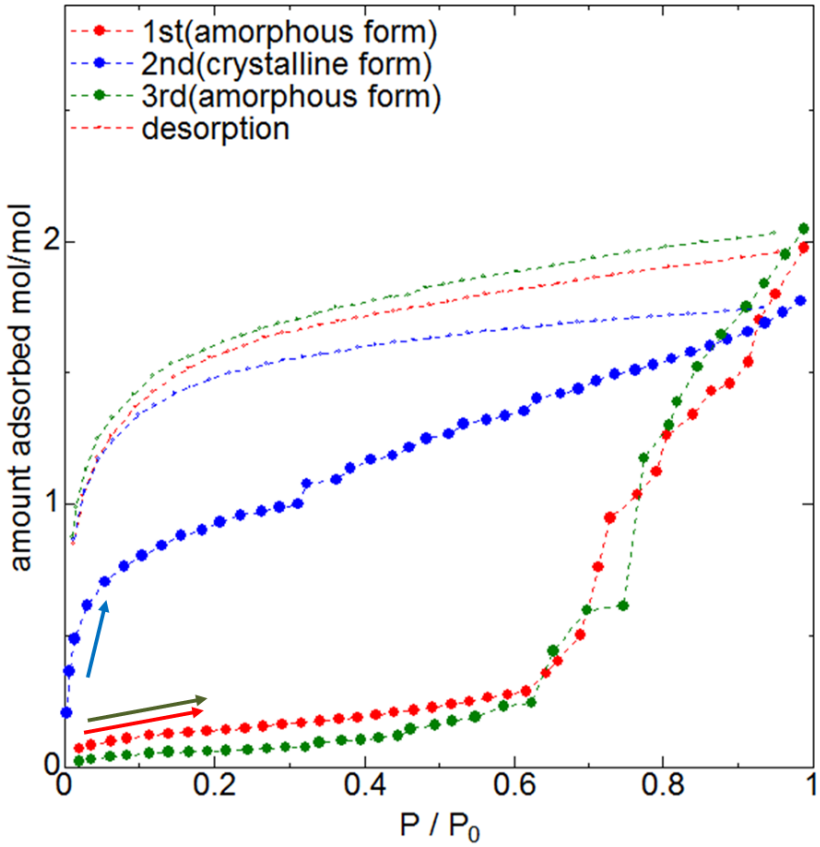

Figure 2-13. EtOH-vapor adsorption isotherms of **1** at 298 K. The same sample was used in these three measurements with different pretreatments. Amorphous form **1P** was used for the first measurement (red). Before the second measurement (blue), the sample was heated *in vacuo* at 120°C to obtain vapor-free crystalline **1R⊃open**. Before the third measurement (green), the sample was heated *in vacuo* at 120°C and then manually ground in a mortar at room temperature to generate the amorphous form **1P**. Closed and open symbols show the adsorption and desorption processes, respectively.

Next, the vapochromic behavior of the red luminescent porous form, **2R⊃open** was examined because the hydrogen bond-supported porous framework may be able to adsorb not only the vapors that induce the amorphous-crystalline transformation from **2P** (e.g., MeOH and EtOH), but also vapors that cannot induce the transformation (e.g., H_2O). Figure 2-14 shows the relative humidity dependence of the luminescence spectrum of the vapor free **2R⊃open** at room temperature. As discussed above, the vapor-free **2R⊃open**, prepared by thermal removal of adsorbed EtOH, showed an emission maximum at 653 nm at room temperature in air, whereas the emission shifted to shorter wavelengths (633 nm) in 100% relative humidity. On the other hand, it shifted to longer wavelengths in lower relative humidity (see Figure 2-14 (b)). In contrast, the luminescence spectrum of the initial nonporous purple form, **2P**, did not change at all upon exposure to water vapor (Figure 2-2). These significantly different results clearly indicate that the blueshifts of the luminescence of the vapor-free **2R⊃open** upon exposure to water vapors originated from water-vapor adsorption which should affect the intermolecular metallophilic interaction in the Pt(II)-stacked chain. To elucidate whether the blueshift of the luminescence of **2R⊃open** originated from H_2O vapor adsorption, H_2O-vapor adsorption isotherms were measured for both the initial amorphous purple form, **2P**, and the vapor-free form, **2R⊃open** (Figure 2-15). Each isotherm was measured after heating at 120ºC in vacuum to remove all the adsorbed solvent molecules. Interestingly, the saturated adsorption amount of **2R⊃open** (ca. 6.1 $molmol^{-1}$ at $P/P_0 = 0.99$) was three times larger than that of **2P** (ca. 2 $molmol^{-1}$ at $P/P_0 = 0.96$). The water-exposed **2R⊃open** has an almost identical structure to **2R⊃water** (Figure 2-16); this noteworthy difference compared with **2P** is likely due to the existence of porous channels in **2R**. In other words, the nonporous amorphous form, **2P**, can adsorb H_2O vapor via the formation of several hydrogen bonds with the hydrophilic carboxyl groups of the H_2dcphen ligands and/or cyanide ligands (i.e., chemisorption). On the other hand, vapor-free **2R⊃open** should be able to adsorb H_2O vapor not only by chemisorption around the hydrophilic groups, but also by physisorption in the porous channels, which enables it to adsorb more H_2O than **2P**. These results indicate that the “molecular-scale shape-memory effect” based on the gate-opening behavior (i.e., **2P** to **2R⊃open**) enables the vapochromic material not only to record past vapor adsorption, but also detect vapors that could not be detected in the gate-closed initial form **2P** (Scheme 2-3).

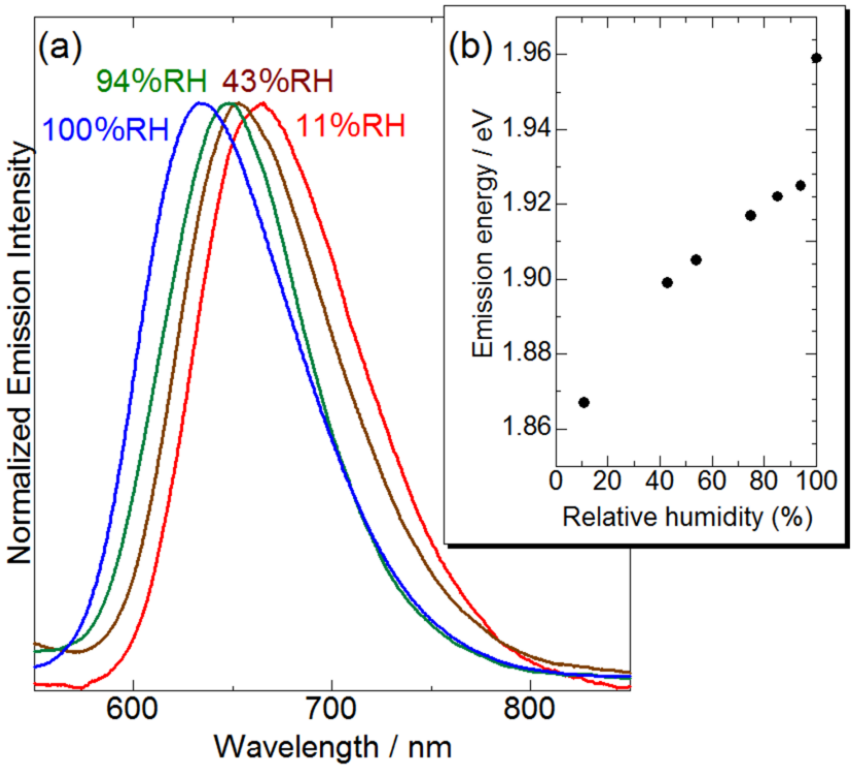

Figure 2-14. (a) Relative-humidity (RH) dependence of the emission spectrum of **2R⊃open** at room temperature (λ_{ex}=400 nm). (b) The relationship between emission energy and relative humidity. The humidity in the quartz cell was controlled by using saturated aqueous solutions of various metal salts.[10)]

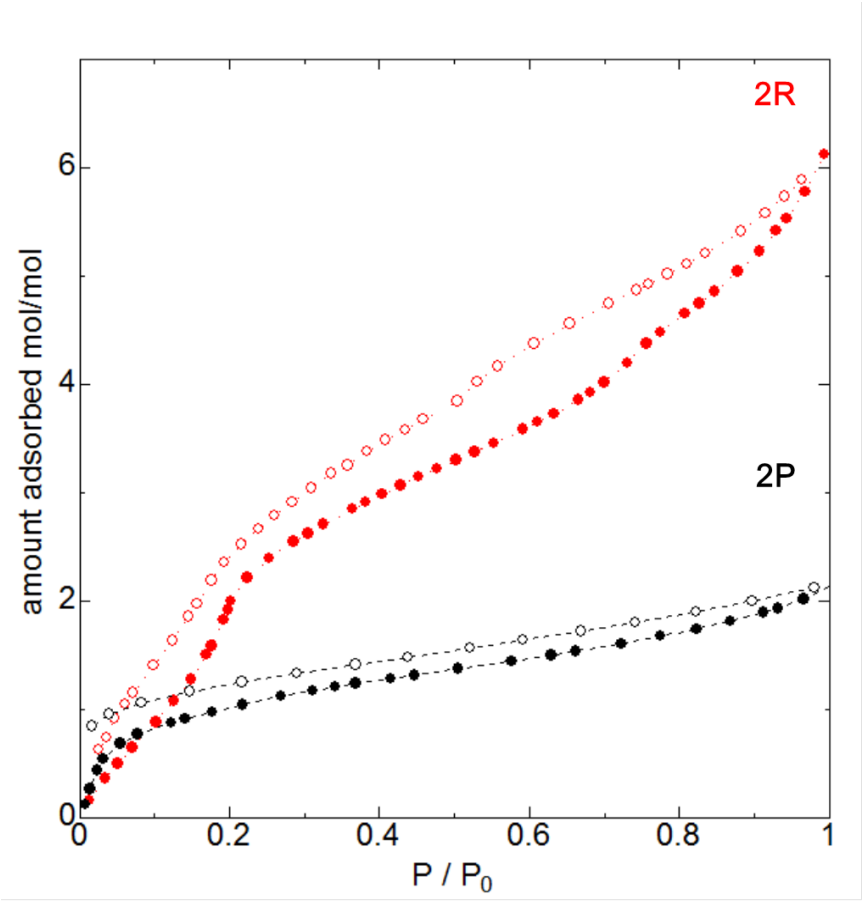

Figure 2-15. Water-vapor adsorption isotherms of **2P** (black) and **2R⊃open** (red) at 298 K. Closed and open symbols show the adsorption and desorption processes, respectively.

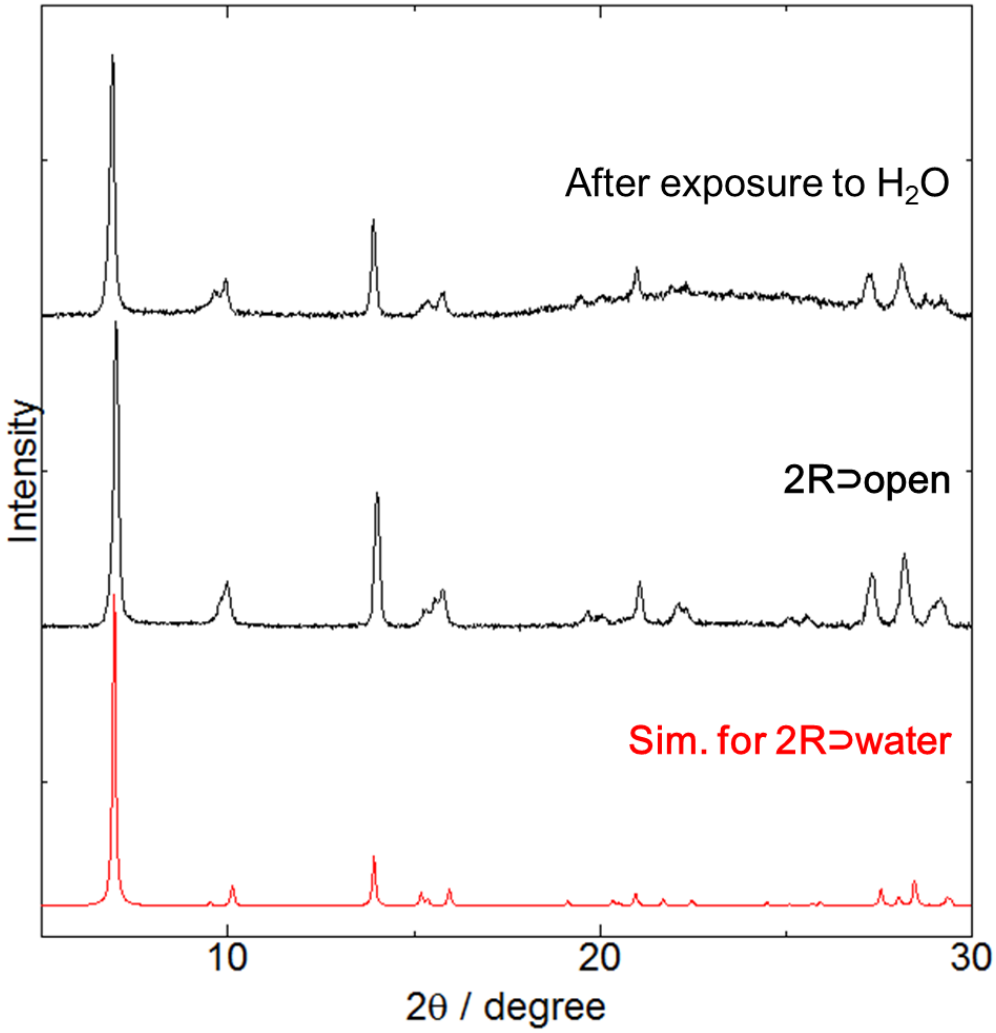

Figure 2-16. Changes of the PXRD pattern of **2R⊃open** after exposure to H_2O vapor. Bottom red line shows the simulation calculated from the crystal structure of **2R⊃water**.

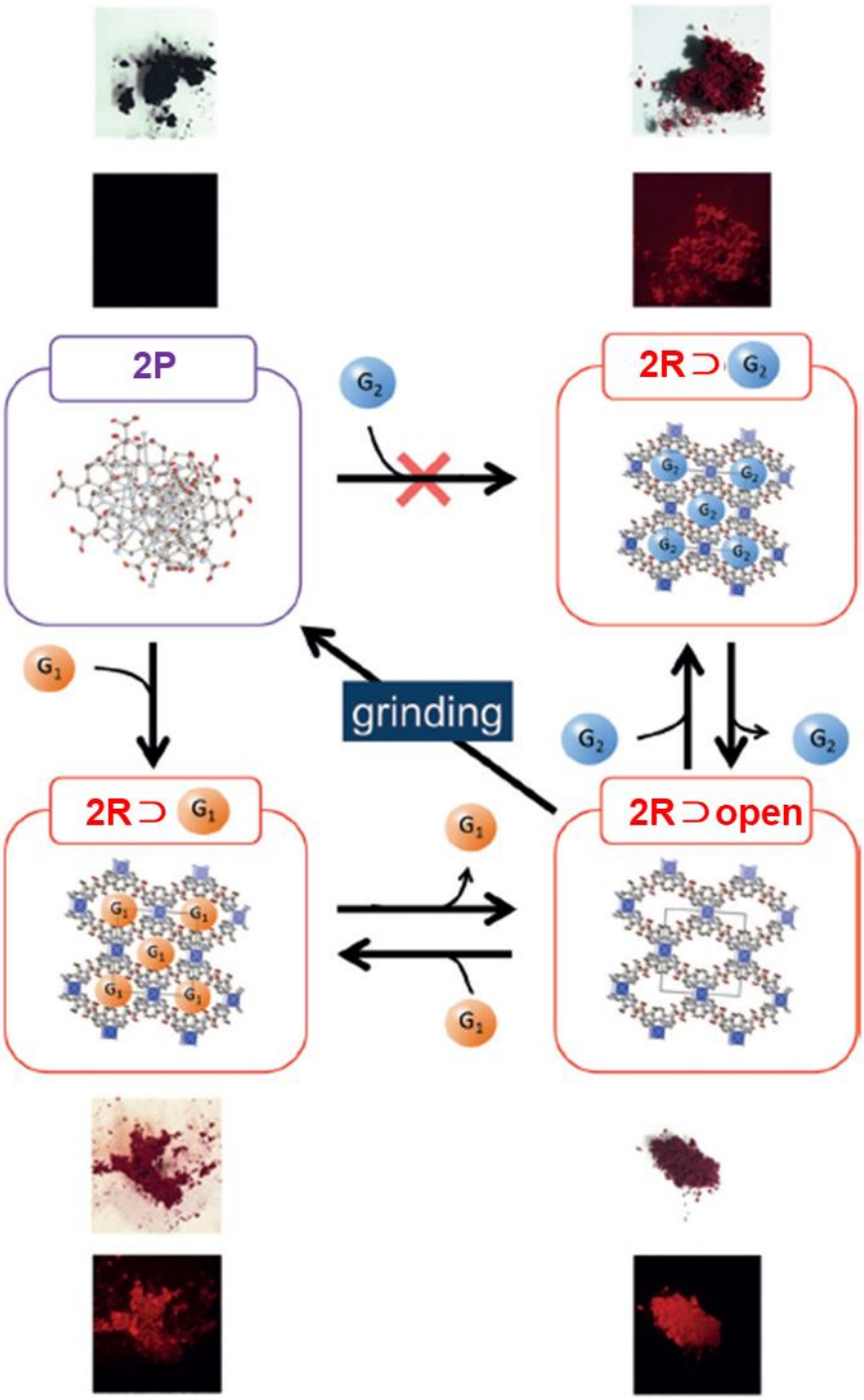

Scheme 2-2. Schematic diagram showing the "molecular-scale shape-memory" behavior of complex **2** based on the vapor-adsorption amorphous-crystalline and grinding driven crystalline–amorphous transformations. Photographs were taken under ambient white light (top) and light irradiation at 533 nm (bottom, a long-pass filter (λ>570 nm) was used).

2-3-4 Thermochromic luminescence

Many Pt(II) complexes with effective metallophilic interactions are known to exhibit temperature-dependent luminescence. Because the red crystalline form, **2R⊃water**, also features effective metallophilic interactions, the luminescence properties are expected to be highly dependent on the temperature. In addition, as mentioned in the crystal structure section, H_2dcphen has a more expanded p-conjugated electronic system than H_2dcbpy, suggesting that the π–π interaction is more effective. To examine the effects of an expanded π conjugation on the thermochromic luminescence behavior, I examined the temperature dependences of both the luminescence spectrum and the crystal structure. Figure 2-17 (a) shows the emission-intensity temperature dependence of **1R⊃water** and **2R⊃water**. The red crystalline form, **2R⊃water**, exhibited a ^{3}MMLCT phosphorescence band at 723 nm (1.72 eV) at 100 K; this band shifted to a shorter wavelength with increasing temperature up to 683 nm (1.84 eV) at 225 K. On the other hand, the bipyridine complex, **1R⊃water**, exhibited the same phosphorescence band as that of **2R⊃water** at 100 K, and exhibited maximum emission at a similar wavelength (686 nm, 1.84 eV) as that of **2R⊃water** at 225 K. Therefore, **2R⊃water** exhibits ^{3}MMLCT phosphorescence at a higher energy than **1R⊃water** does in this temperature range. In addition, the temperature dependence of the ^{3}MMLCT band energy of **2R⊃water** is less pronounced than that of **1R⊃water**. To clarify the origin of these differences, the temperature dependences of the intermolecular Pt···Pt distances of these two complexes were estimated from the single-crystal X-ray diffraction measurements. The crystallographic parameters at each temperature are summarized in Table 2-1. Single-crystal X-ray diffraction analysis was conducted with the same single crystal at various temperatures. Figure 2-17 (b) shows the temperature dependences of the energy of the ^{3}MMLCT band and intermolecular Pt···Pt distances of **1R⊃water** and **2R⊃water**. The intermolecular Pt···Pt distance of **2R⊃water** expended from 3.2355(3) Å at 100 K to 3.2768(8) Å upon a temperature increase to 225 K, whereas the Pt···Pt distance of **1R⊃water** (3.2161(6) Å) was 0.019 Å shorter than that of **2R⊃water** at 100 K and expanded to a similar distance (3.2642(6) Å) as that of **1R⊃water** at 225 K. The different temperature dependences of the intermolecular Pt···Pt distances of **1R⊃water** and **2R⊃water** is in good agreement with the temperature dependence of the ^{3}MMLCT band energy of these complexes: **2R⊃water** exhibited higher-energy phosphorescence and less pronounced temperature dependence than **1R⊃water**, because of weaker intermolecular Pt···Pt interactions. The cell lengths along the c axis corresponding to the direction of the intermolecular Pt···Pt interactions of these complexes are very similar in this temperature range (Figure 2-18); this result implies that the differences in the molecular shapes of the H_2dcphen and H_2dcbpy ligands does not affect the thickness of the square-planar Pt(II) complex molecule. Consequently, the weaker intermolecular Pt···Pt interactions of **2R⊃water** than those of **1R⊃water** are likely to

originate from the more distorted Pt···Pt stacking structure. In fact, the Pt···Pt···Pt stacking angle of **2R⊃water** is smaller than that of **1R⊃water** in this temperature range (Figure 2-18). Moreover, in spite of longer Pt···Pt distances in **2R⊃water** than in **1R⊃water**, the distances between the diamine and cyanide ligands are almost same (Table 2-2). These are partially caused by the more expanded π-conjugated ligand in **1** than in **2**, that is, the H_2dcphen ligand may enhance the intermolecular π–π stacking interactions between the diimine and cyanide ligands, resulting in weaker intermolecular Pt···Pt interactions and a higher-energy emission band of **2R⊃water** as compared with those of **1R⊃water** (Figure 2-17 c).

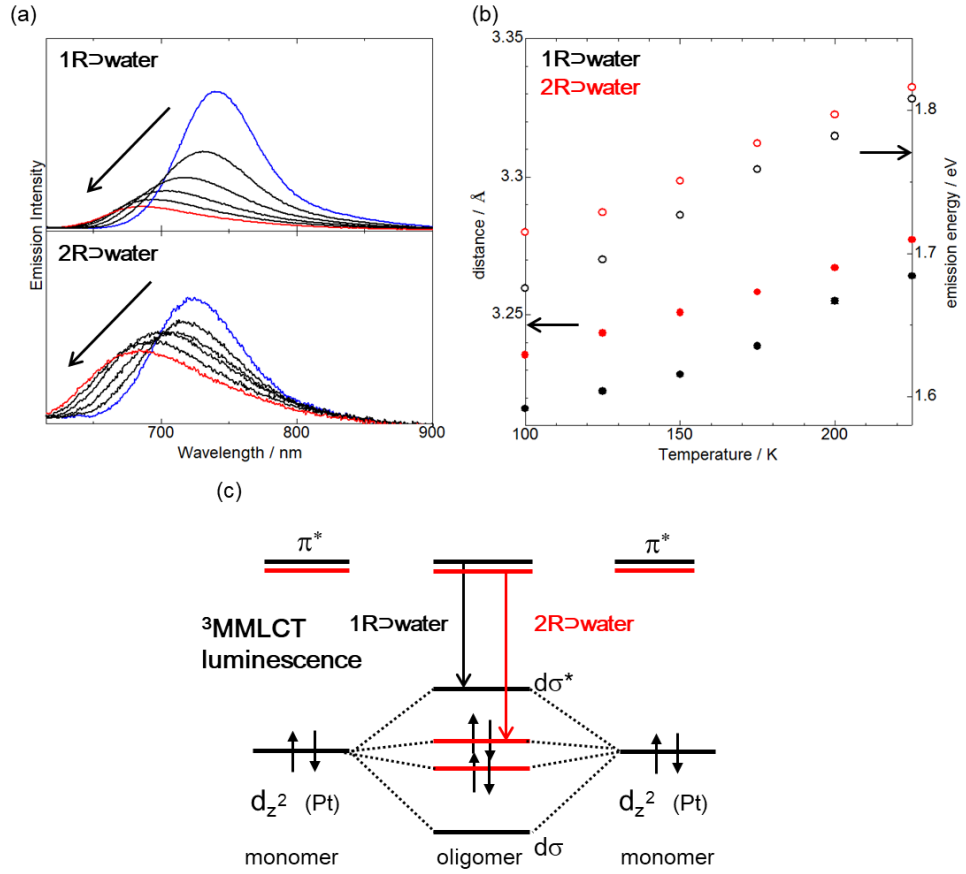

Figure 2-17. (a) The temperature dependence of the luminescence spectra (λ_{ex}=400 nm) of **1R⊃water** (top) and **2R⊃water** (bottom) from 100 K(blue) to 225 K(red). (b) The temperature dependences of the Pt···Pt distances (closed symbols) and luminescence energies (open symbols) of **1R⊃water** (black) and **2R⊃water** (red). The Pt···Pt distances were estimated by single-crystal X-ray structural analysis. (c) Schematic luminescence energy diagrams of **1R⊃water** and **2R⊃water**.

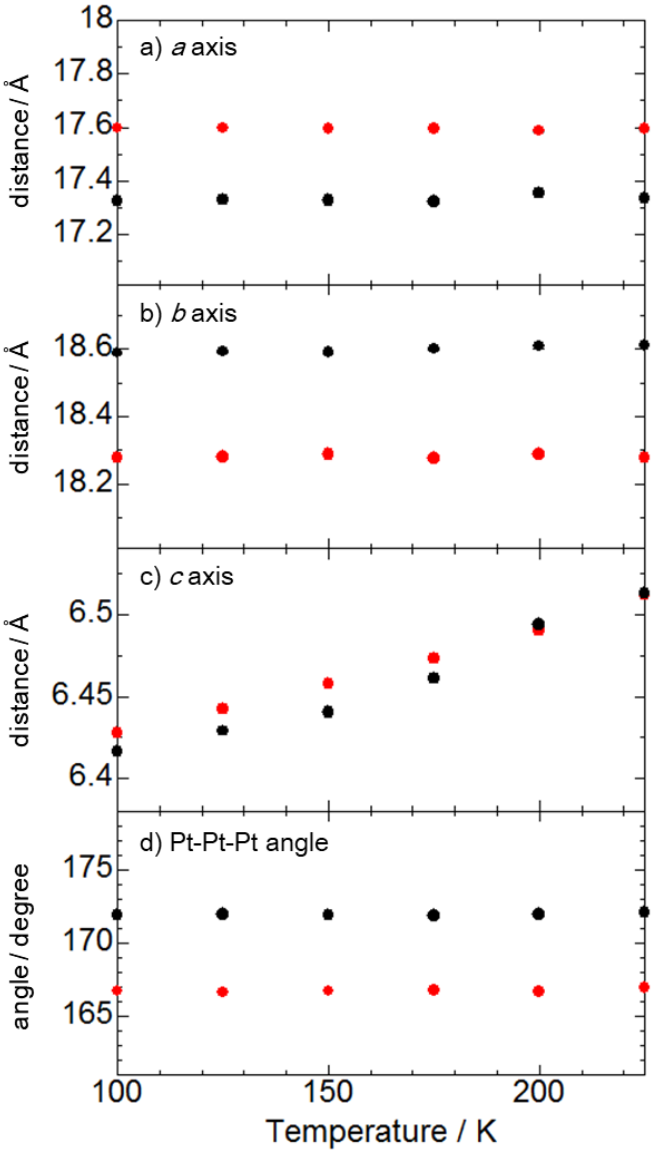

Figure 2-18. Temperature dependence of (a) *a* axis, (b) *b* axis, (c) *c* axis and (d) Pt-Pt-Pt angle for **1R⊃water** (black) and **2R⊃water** (red) estimated by single crystal X-ray diffraction analysis.

2-4 Conclusion

A new Pt(II)-diimine complex, $[Pt(CN)_2(H_2dcphen)]$ (**2**; H_2dcphen = 4,7-dicarboxy-1,10-phenanthroline) was successfully synthesized, and found that it shows a unique vapochromic behavior with vapor-history sensing and ON–OFF-switching functions derived from the "molecular-scale shape-memory" behavior of the porous framework. The crystal structure is isomorphic to the bipyridine analogue, $[Pt(CN)_2(H_2dcbpy)]$ (**1** ; H_2dcbpy = 4,4'-dicarboxy-2,2'-bipyridine), and has a similar porous structure. The purple amorphous form of the complex, **2P**, shows drastic color/luminescence changes upon exposure to several alcoholic vapors. These vapor-induced color/luminescence changes of **1P** originate from a structural transformation to the red crystalline **2R⊃vapor**, which contains adsorbed vapor molecules in the porous channels. A noteworthy difference between **1P** and **2P** was observed upon exposure to *t*-BuOH vapor: Only **1P** showed a drastic color change from purple to red, suggesting that the pores of **2R** are too small to adsorb *t*-BuOH vapor. Interestingly, the crystalline porous structures of both **1R⊃vapor** and **2R⊃vapor** constructed by vapor adsorption are retained after thermal removal of the vapor molecules to form the vapor-free phases, **1R⊃open** and **2R⊃open**, respectively, although the color/luminescence changes because of changes to the intermolecular metallophilic interactions. These vapor-free phases collapse as a result of manual grinding in a mortar to regenerate the initial purple amorphous forms, **1P** and **2P**. The temperature dependence of the luminescence spectra of **2R** indicates that the luminescence of **2R** is due to ^{3}MMLCT emission, similar to that of **1R**. However, the weaker temperature dependence of **2R** may be due to enhanced intermolecular π–π stacking interactions caused by the more expanded p conjugation of the H2dcphen ligand compared with that of that the H_2dcbpy ligand, which would compete with the intermolecular Pt⋯Pt interactions. These results clearly indicate that Pt(II)-diimine supramolecular systems, such as **1** and **2**, are not only multichromic materials that respond to various external stimuli, but also a new type of vapor-history sensing materials with ON-OFF switching functions based on the "molecular-scale shape-memory" ability derived from the formation and collapse of the porous structure by vapor adsorption and manual grinding, respectively. This work has been published on Chemistry A European Journal.[11)]

2-5 References

(1) a) A. Kobayashi and M. Kato, *Eur. J. Inorg. Chem.*, **2014**, 4469–4483. b) C. Jobbágy and A. Deák, *Eur. J. Inorg. Chem.*, **2014**, 4434–4449.

(2) M. Kato, S. Kishi, Y. Wakamatsu, Y. Sugi, Y. Osamura, T. Koshiyama and M. Hasegawa, *Chem. Lett.* **2005**, *34*, 1368-1369.

(3) M. Yanagida, L. P. Singh, K. Sayama, K. Hara, R. Katoh, A. Islam, H. Sugihara, H. Arakawa, M. K. Nazeeruddin and M. Grätzel, *J. Chem. Soc. Dalton Trans.,* 2000, 2817-2822.

(4) H. Wolpher, S. Sinha, J. Pan, A. Johansson, M. J. Lundqvist, P. Persson, R. Lomoth, J. Bergquist, L. Sun, V. Sundstrcm, B. Akermark and T. Polivka, *Inorg. Chem.,* **2007**, *46*, 638-651.

(5) CrystalClear; Molecular Structure Corporation: Orem, UT, **2001**.

(6) SIR2004: M. C. Burla, R. Caliandro, M. Camalli, B. Carrozzini, G. L. Cascarano, L. De Caro, C. Giacovazzo, G. Polidori and R. Spagana, *J. Appl. Crystallogr.* **2005**, *38*, 381-388.

(7) SHELX97: G. M. Sheldrick, *Acta Crystallogr. Sect. A,* **2008**, *64*, 112-122.

(8) TOPAS v4.2, general profile and structure analysis software for powder diffraction data. Bruker AXS, Karlsruhe, Germany, **2011**.

(9) Y. Sakata, S. Furukawa, M. Kondo, K. Hirai, N. Horike, Y. Takashima, H. Uehara, N. Louvain, M. Meilikhov, T. Tsuruoka, S. Isoda, W. Kosaka, O. Sakata and S. Kitagawa, *Science*, **2013**, *339*, 193-196.

(10) H. L. Goderis, B. L. Fouwe, S. M. Van Cauwebergh and P. P. Tobback, *Anal. Chem.* **1986**, *58*, 1561-1563.

11) Y. Shigeta, A. Kobayashi, T. Ohba, M. Yoshida, T. Matsumoto, H.-C. Chang and M. Kato, *Chem. Eur. J.*, **2016**, *22*, 2682-2690.

Chapter 3

Vapochromic Pt(II) Complexes Having Vapor-History Sensing Ability

3-1 Introduction

In most of Type I vapochromic compounds, the color change originates from the structure transformation induced by vapor adsorption, and the original (= initial) color was recovered by the removal of the adsorbed vapor because of the lack of structural stability of the vapor-adsorbed form.[1)] These compounds are useful as the *in-situ* vapor detection. On the other hand, as discussed in Chapter 2, the vapochromic complex **2**, $[Pt(CN)_2(H_2dcphen)]$ can retain the characteristic color for vapor-adsorbed form *even after* the removal of adsorbed vapor molecules in the porous channels.[2)] Moreover, this stable porous structure can be collapsed by grinding. Similar behavior has been reported by Kitagawa and co-workers.[3)] In the paper, they described that relationship between vapor ad/desorption process and crystal structures for the various size of the PCP, $[Cu_2(bdc)_2(4,4'\text{-bpy})]_n$ (bdc=1,4-benzenedicarboxylate, 4,4'-bpy = 4,4'-bipyridine). Upon vapor adsorption, the PCP exhibited transformation from original (closed) shape to temporary (opened) shape. However, the temporary shape was retained after gas desorption in case of using down-sized crystal. Moreover, the temporary shape can be recovered by heating. This "molecular-scale shape-memory" behavior enabled **2** to not only *in situ* vapor detection, but also vapor *history* sensing. However, the luminescence wavelength of the *vapor-memorized* red crystalline form **2** (abbreviated as a **2-Rc**, capital letter means its color and small letter means its form; **c**rystalline or **a**morphous-like solid) changed easily in ambient atmosphere, because **2-Rc** is porous and can adsorb H_2O vapor in ambient air. From the viewpoint of the vapor history sensing, this variable emission character of **2-Rc** for H_2O vapor would be the weak point, because it makes difficult to distinguish whether the color change was triggered by the *past* vapor adsorption process or by the *in-situ* vapor adsorption.

In this chapter, to examine the extensibility of the "molecular-scale shape-memory" behavior and the stability of porous structure, the complex **3**, $[Pt(CN)_2(H_2dpcpbpy)]$ ($H_2dpcpbpy$ = 4,4'-di(*p*-carboxyphenyl)-2,2'-bipyridine) was newly synthesized to extend the pore size of complex **1** and the vapochromic behavior was investigated in detail.

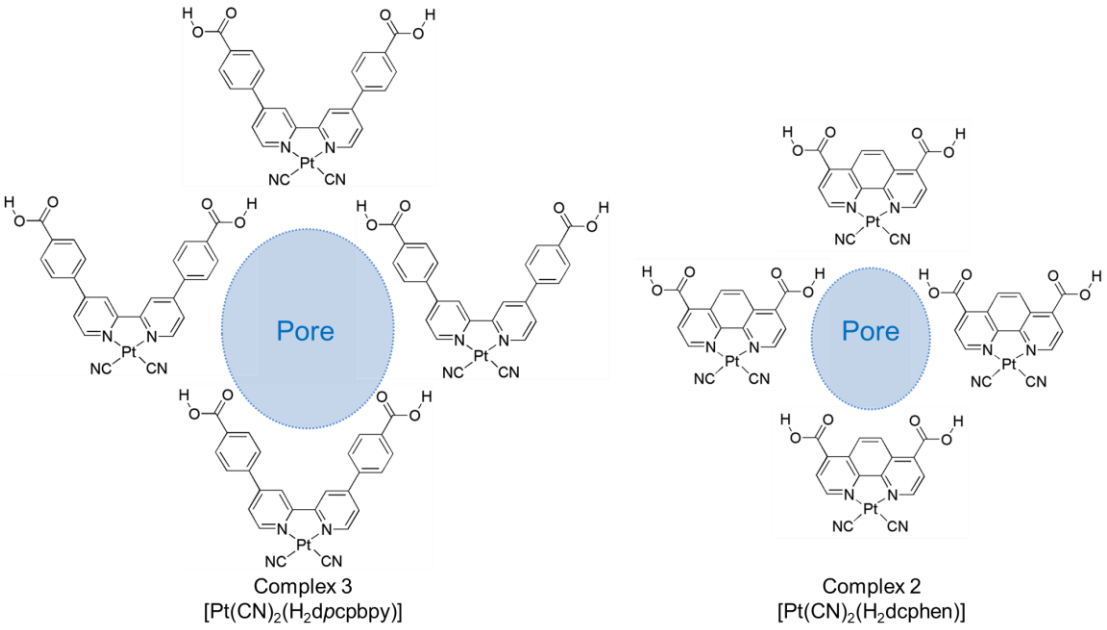

Scheme 3-1. Molecular structure and expected hydrogen bonding formation of complex **3** and **2**.

3-2 Experimental section

3-2-1 Materials and methods

General procedures

All commercially available starting materials were used without any purification. The precursor materials, 4,4′-dibromo-2,2′-bipyridine,[4,5,6] 4-carboxyphenylboronic acid,[7] $Pd(PPh_3)_4$[8] and $Pt(CN)_2$[9] were prepared according to previously published methods. The ^1H NMR spectrum of each sample was measured using a JEOL EX-270 NMR spectrometer at room temperature. Elemental analysis was conducted at the analysis center at Hokkaido University.

Synthesis of H_2d*p*cpbpy

Na_2CO_3 (1.68 g, 16.0 mmol) was added to the solvent mixture of H_2O (80 ml) and methanol (96 ml). 4,4′-dibromo-2,2′-bipyridine (1.20 g, 3.83 mmol) was added to the mixture, and then resulting suspension was bubbled by N_2 for 30 minutes. The mixture was purged by N_2, and 4-carboxyphenylboronic acid (1.26 g, 9.70 mmol) and $Pd(PPh_3)_4$ (480 mg, 0.4 mmol) were added. The resulting mixture was heated to reflux for 3 days under N_2 atmosphere and the obtained reaction mixture was filtered off and then the filtrate was evaporated to dryness. The residue was suspended in H_2O(50 ml) and subsequently added to dil. HCl aq. to acidify. The resulting white suspension was centrifuged, washed with H_2O, MeOH, acetone. After drying under reduced pressure, the target ligand, H_2d*p*cpbpy was obtained as a white powder. Yield: 1.08 g, 71%. This compound was used for next synthesis without further purification. ^1H NMR (270 MHz, NaOD in CD_3OD/D_2O): δ = 8.80 (d, 2H), 8.58(s, 2H), 8.11(d, 4H), 7.91(d, 4H), 7.88(d, 2H)

Synthesis of yellow amorphous [$Pt(CN)_2$(H_2d*p*cpbpy)] (=3-Ya)

This complex was synthesized by the slightly modified synthetic procedure of the complex **2**.[1] $Pt(CN)_2$ (480 mg, 1.94 mmol) was suspended in conc. NH_3 aq. (98 ml). H_2d*p*cpbpy (385 mg, 0.97 mmol) was added to the mixture, and then the resulting suspension was heated at 100°C for 2 days. After the reaction, the obtained suspension was filtered off. The filtrate was added to dil. HNO_3 aq. and yellow precipitate was emerged. The yellow precipitate was collected by filtration and washed with H_2O and dried under vacuum to afford the target compound as the yellow powder (**3-Ya**). Yield: 460 mg, 73%. ^1H NMR (270 MHz, DMSO-d_6) δ= 9.28 (s, 2H), 9.21 (d, 2H), 8.35 (d, 2H), 8.25 (d, 4H), 8.19 (d, 4H); elemental analysis calcd. For $C_{26}H_{16}N_4O_4Pt\cdot(9H_2O)$: C 38.76, H 4.25, N 6.95; found: C 38.85, H 3.97, N 7.25.

Synthesis of orange crystal [$Pt(CN)_2$(H_2d*p*cpbpy)]·3H_2O (=3-Oc)

To the suspension of [$Pt(CN)_2$(H_2dpcpbpy)] 0.25 mg (4 μmol) in methanol (7 ml), the

methanolic solution of lithium methoxide (10% solution in methanol, 25 μl) was added. Diffusion of acetic acid vapor into the methanol solution at 30°C for 2 days gave **3-Oc** as orange crystals suitable for single crystal X-ray diffraction study.

3-2-2 Physical measurements

Powder X-ray diffraction (PXRD).

Powder X-ray diffraction was conducted using a Rigaku SPD diffractometer at beamline BL-8B at the Photon Factory, KEK, Japan or a Bruker D8 Advance diffractometer equipped with a graphite monochrometer using Cu-Kα radiation and one-dimensional LinxEye detector. The wavelength of the synchrotron X-ray was 1.5385(1) Å.

Luminescence properties.

The luminescence spectrum of each complex was measured using a JASCO FP-6600 spectrofluorometer at room temperature. Typical slit width of the excitation and emission light were 5 and 6 nm, respectively.

UV-Vis Spectroscopy.

The UV-Vis diffuse reflectance spectrum of each complex was recorded on a Shimadzu UV-2400PC spectrophotometer.

Vapor adsorption isotherms.

The vapor adsorption isotherms of each complex were measured using a BELSORP-max vapor adsorption isotherm measurement equipment at 298 K.

Single-crystal X-ray diffraction measurement: The measurement for **3-Oc** were conducted with a Rigaku Mercury CCD diffractometer with monochromated MoKa radiation (λ= 0.71069 Å) and a sealed X-ray tube generator. The single crystal was mounted on a MicroMount coated with paraffin oil. The crystal was then cooled by using an N_2 flowtype temperature controller. The diffraction data were collected and processed with Crystal-Clear software.[10] The structures were solved with the direct method by using SHELXS2013.[11] Structural refinements were conducted by the full-matrix least-squares method with SHELXL2013.[11] Nonhydrogen atoms were refined anisotropically, and all hydrogen atoms were refined with the riding model. All calculations were conducted with the Crystal Structure crystallographic software package.

3-3 Result and discussion

3-3-1 Synthesis and Characterization

Although **3** was successfully synthesized by almost the same synthetic procedure to that of **2**, **3** was obtained as the yellow-colored powder (**3-Ya**) which showed completely different color to that of the purple form of **2-Pa**. To elucidate the difference between **3-Ya** and **2-Pa**, PXRD, UV-Vis absorption and diffuse reflectance spectral measurements were conducted. Obtained PXRD pattern for **3-Ya** was featureless without any sharp diffraction peaks, indicating that **3-Ya** is amorphous-like solid as well as **2-Pa** (See Figure 3-2). On the other hands, as shown in Figure 3-1, UV-Vis absorption spectra of these complexes showed obvious difference. The complex **2-Pa** in solution exhibited absorption band ranging up to 400 nm whereas the broad absorption band extended to 700 nm was observed in the UV-Vis diffuse reflectance spectrum of the amorphous-like solid **2-Pa**. This result clearly indicated that intermolecular interactions such as Pt-Pt interaction contribute to the electronic transition of **2-Pa** in solid state. Similarly, **3-Ya** exhibited obvious absorption band at around 340 nm in the solution state, and it extended to longer wavelength side up to 500 nm in the solid state. This result also suggests the contribution of the intermolecular interaction to the electronic transition of the amorphous-like solid **3-Ya**. The higher molar absorption coefficient of **3-Ya** than that of **2-Pa** in solution state is due to the more expanded π conjugation of H_2d*pc*pbpy ligand than that of H_2dcphen ligand. It should be noted that observed absorption band of **3-Ya** in the solid state was located at shorter wavelength than that of **2-Pa**. It suggests that the intermolecular interaction of **3-Ya** is weaker than that of **2-Pa**. This difference is probably due to the steric effect of the newly introduced phenyl ring which can rotate along the C-C bond to weaken the intermolecular interaction.

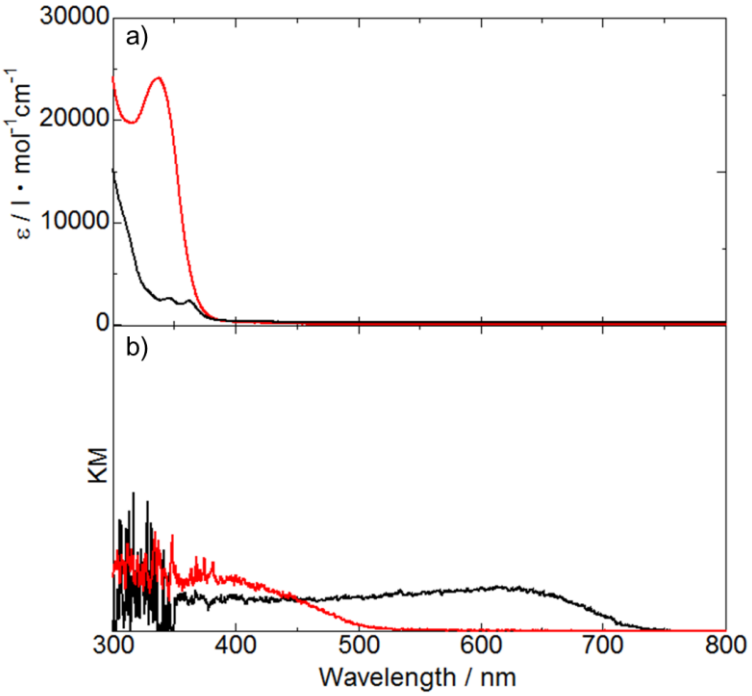

Figure 3-1. (a) Solution-state UV-Vis absorption and (b) Solid-state UV-Vis diffuse reflectance spectra of **3-Ya** (red lines) and **2-Pa** (black lines). In the absorption spectral measurements, DMSO was used as the solvent for **3**, but NH_3 aq. (2.8%) was used for **2** because of the low solubility of **3** for diluted NH_3 aq.

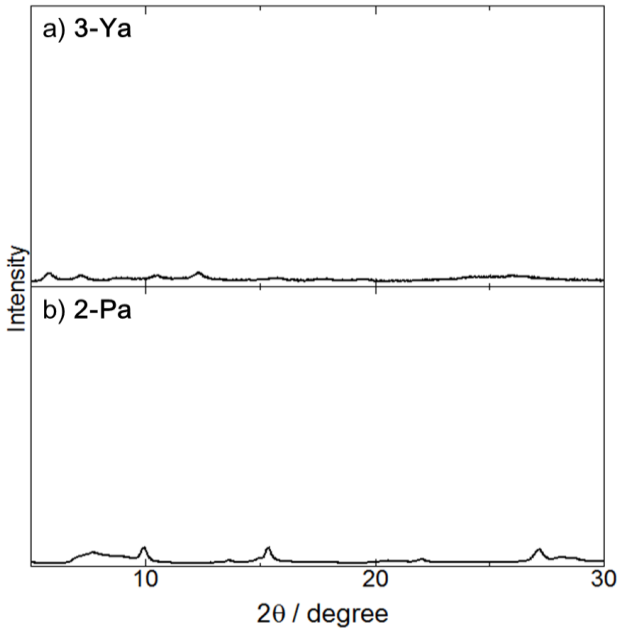

Figure 3-2. PXRD patterns of **3-Ya**(a) and **2-Pa**(b).

3-3-2 Crystal structure of $[Pt(CN)_2(H_2dpcpbpy)]\cdot 3H_2O$(3-Oc)

Figure 3-3 displays the crystal structure of the orange crystalline form **3** (named as **3-Oc**). Crystallographic data and selected bond length angles of **3-Oc** are listed in Tables A and B, respectively. **3-Oc** was found to be crystallized in the same space group (*Cmcm*) as **2-Rc**. In this structure, the half of one molecule was crystallographically independent due to the mirror plane of this space group. The Pt(II) center of **3-Oc** was coordinated by two N atoms from H_2dpcpbpy ligand and two C atoms from the two cyanide ligands to form the typical square-planar coordination geometry. The bond lengths around Pt(II) center in **3-Oc** were almost comparable to that in **2-Pa**, suggesting the negligible effect of the introduction of phenyl group between the bpy ligand and the carboxy groups. The two different C-O bond lengths of the carboxy group (1.27(4) and 1.11(5) Å) indicated that the O atom with the longer C-O bond distance is protonated. The short distance between the O atom of carboxylic acid group and the nitrogen of cyanide ligand of the adjacent molecule (O-H···N: 2.69(3) Å) suggests the tight hydrogen bond between them. As the result, the similar two-dimensional hydrogen bonding network structure to that of **2-Rc** was constructed in the *ab* plane. As shown in Figure 3-3(b), this square-planar molecule stacked one-dimensionally along the *c* axis with the anti-parallel orientation of the phenyl carboxy groups attached on the bpy moiety. The intermolecular Pt-Pt distance (3.353(2) Å) was shorter than the twice of van der Waals radius of Pt atom (3.5 Å), clearly indicating the effective Pt-Pt interaction in this stacked structure. Notably, this intermolecular Pt-Pt distance in **3-Ya** was longer than that of **2-Rc** despite the almost linear stacking manner, that is, the Pt-Pt-Pt stacking angle in **3-Ya** was closer to 180 deg. than that of **2-Rc**. Thus, the intermolecular Pt-Pt interaction in **3-Ya** is weaker than that in **2-Rc**, probably due to the steric effect of the phenyl ring attached on the 4- and 4′- positions of bpy moiety. Since these phenyl groups between the bpy and carboxy groups were also stacked along the *c* axis with the relatively short distance (3.350 Å,) the intermolecular π–π stacking interaction is also effective in this structure. As the results of 2-D hydrogen bonding network in the *ab* plane and the intermolecular Pt-Pt and π-π stacking interactions along the *c* axis, the large porous channel structure was formed in **3-Oc** as well as **2-Rc**. As expected from the molecular structure of **3**, the pore size (14.3 × 8.6 $Å^2$) and void fraction (48.7%) of **3-Oc** were larger than those of **2-Rc** (6.4 × 6.8 $Å^2$ and 35.2%). In this large void space, four crystal water molecules were found and two of them were directly hydrogen bonded to the O atom of the carboxy group of **3** with the 2.84(3) Å (Figure 3-4).

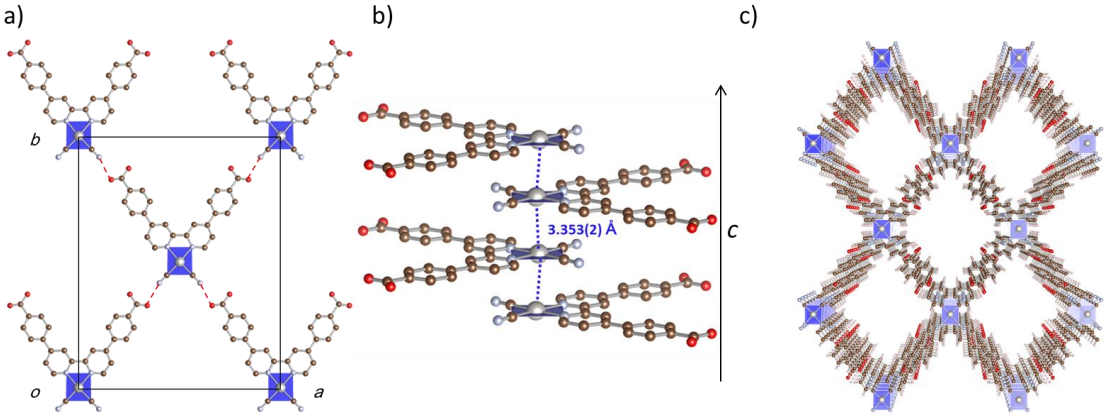

Figure 3-3. Crystal structure of **3**. 2-D hydrogen bonding crystal structure in the ab plane (a), 1-D Pt-Pt interaction along the *c* axis (b) and porous structure (c). Solvent molecules and hydrogen atoms are omitted for clarity.

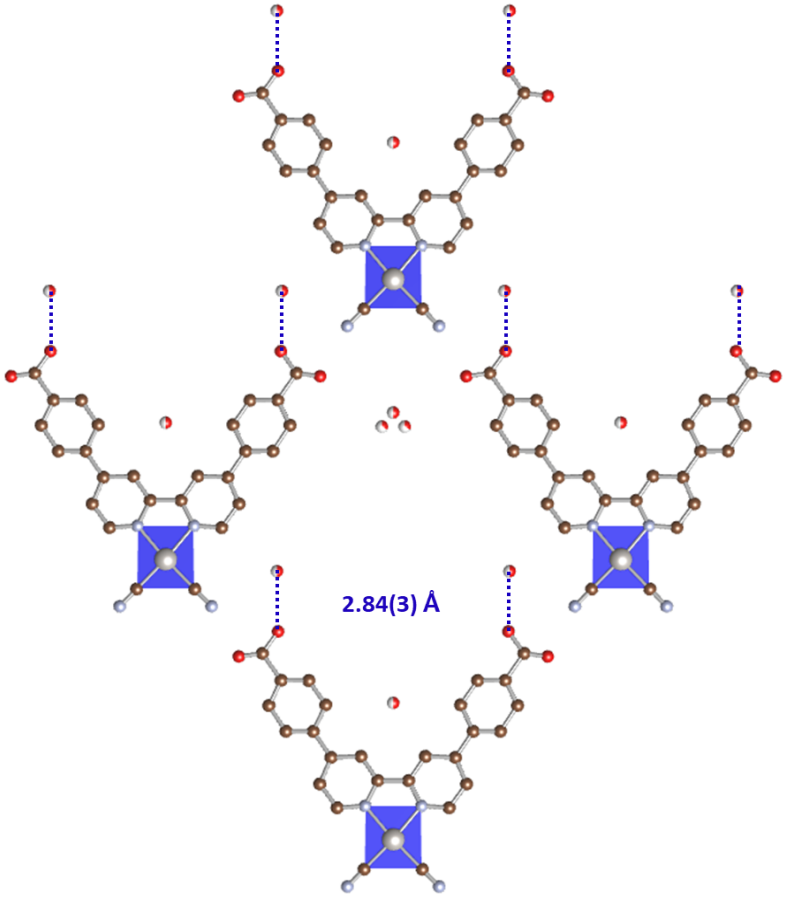

Figure 3-4. Positions of water molecules in the porous structure of **3**. Hydrogen bonding between C-O bond and water molecules were indicated by blue dotted lines.

Table 3-1. Crystal parameters and refinement result for **3** in comparison with those of **2**. Void fraction was calculated by SQUEEZE program.

Complex	**3**	**2**
T / K	200	200
Formula	$PtC_{26}H_{16}N_4O_4$	$PtC_{16}H_8N_4O_7$
Formula weight	643.5	563.35
Crystal system	Orthorhombic	Orthorhombic
Space group	*Cmcm*	*Cmcm*
a / Å	21.22(1)	17.587(4)
b / Å	26.43(1)	18.288(5)
c / Å	6.699(4)	6.4903(15)
α/ deg.	90	90
β / deg.	90	90
γ/ deg.	90	90
V / Å^3	3756(3)	2087.5(9)
Z	4	4
D_{cal}/ g·cm^{-3}	1.226	1.812
Reflections collected	14364	12292
Unique reflections	2394	1445
GOF	1.096	1.082
R_{int}	0.1099	0.0828
R (I > 2.00σ(I))	0.0797	0.0326
R_W [a]	0.1976	0.0805
Pore diameter	14.3 × 8.6 Å^2	6.4×6.8 Å^2
Void fraction	48.7 %	35.2%

[a] $R_W = [\Sigma(w(F_o^2 - F_c^2)^2)/\Sigma w(F_o^2)^2]^{1/2}$.

Table 3-2. Selected bond lengths and angles for complexes **3** and **2**.

Complex	**3**	**2**[a]
T / K	200	200
Pt1-N1	2.06(1)	2.047(5)
Pt1-C7	1.95(1)	1.962(5)
O1-H···N3	2.69(3)	2.665(8)
Pt1···Pt1	3.353(2)	3.2668(7)
Pt1···Pt1···Pt1	174.90(2)	166.80(1)

[a] Ref.2

3-3-3 Vapor-adsorption-triggered structure transformation

As mentioned in Introduction, **2** exhibited color changing from purple to red originated from amorphous-crystalline transformation triggered by EtOH vapor adsorption. Since **3-Oc** has very similar porous structure to **2-Rc**, we have investigated about the vapochromic behavior of the complex **3**. Figure 3-5(a) shows the PXRD pattern changes of the yellow amorphous-like solid **3-Ya** upon exposure to EtOH, and the following heat and grind treatments. The initial broad amorphous like pattern of **3-Ya** drastically changed to the diffraction pattern with many sharp peaks by exposing it to EtOH vapor. The observed PXRD pattern is qualitatively consistent with the simulation pattern of **3-Oc**. This result indicates that the amorphous-crystalline transformation from the amorphous-like solid **3-Ya** to the EtOH-adsorbed crystalline porous phase **3-Oc**⊃EtOH occurred by exposing it to EtOH vapor as well as the case of **2-Pa** (see Figure 3-5(b)). On the other hands, most of the diffraction peaks except for several peaks at low angle region were disappeared after the heating **3-Oc**⊃EtOH at 120°C for 3 h. In this heating condition, most of the adsorbed EtOH molecules in **3-Oc**⊃EtOH were removed as confirmed by thermogravimetric analysis (Figure 3-6). This result indicates that the porous crystal structure of **3-Oc** was collapsed by desorption of EtOH vapor, whereas the porous structure of **2-Ra** retained even after the removal of EtOH in the almost the same heating condition. Thus, the porous structure of **3-Oc** was not stable enough to retain it without the adsorbed EtOH molecules, and the less stability of **3-Oc** than **2-Rc** would be due to the expanded porous structure with larger void fraction and weaker intermolecular hydrogen-bonding interaction (see Tables 3-1 and 3-2). To elucidate further effect for expanding pore size, the amount of adsorbed molecules for complex **2** and **3** were determined and shown in Table 3-3. Adsorbed EtOH amount were slightly decreased by expanding pore size, maybe due to fast collapse of porous crystal structure. However, adsorbed amount for H_2O molecule was drastically increased. This difference was probably due to the expanding pore size. Therefore, complex 3 can adsorb more vapor molecules than complex 2, by using its expanded pores.

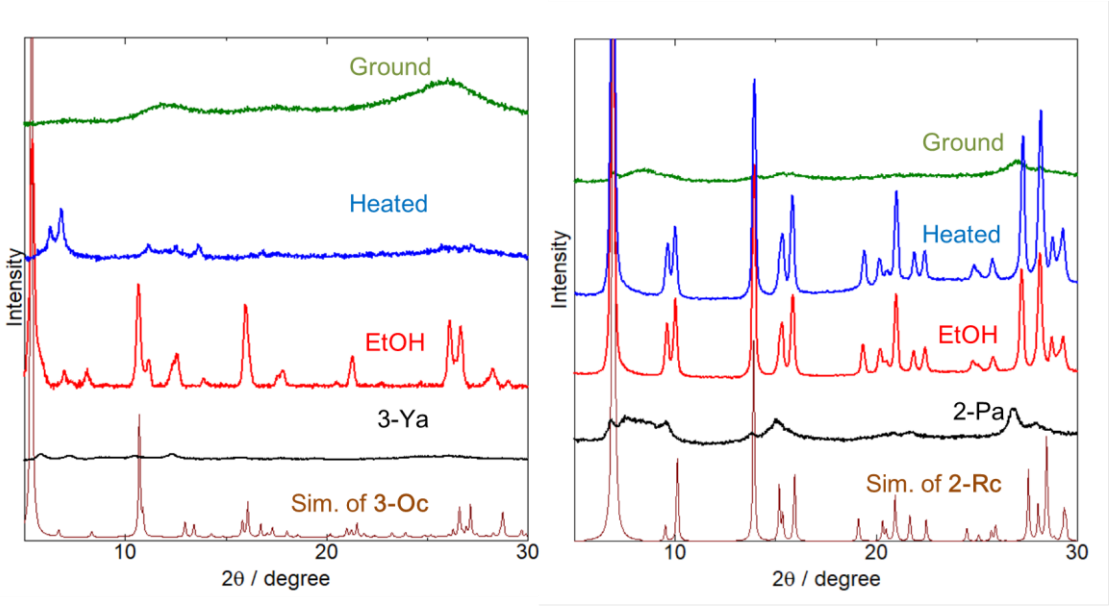

Figure 3-5. Changes of powder X-ray diffraction patterns of (a) **3** and (b) **2**. Each amorphous form (black lines) was exposed to EtOH vapor for 5 days at 303 K (red lines). Then, the EtOH form was heated at 120°C for 2 hours (blue lines). Finally, the heated sample was ground manually using mortar (green lines). The orange lines show the simulation patterns of the crystal structures determined by single crystal X-ray structure analysis.

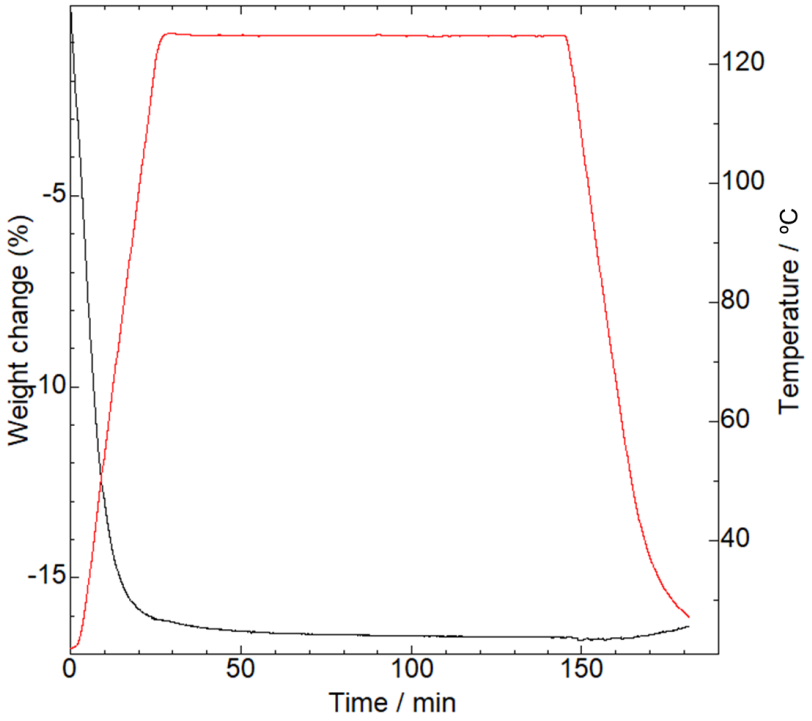

Figure 3-6. Thermogravimetric analysis for **3-Oc⊃EtOH**. Thermogravimetric analysis for the EtOH adsorbed **3-Oc**. -16.6% of weight loss is corresponded to $3 \cdot 0.7EtOH \cdot 5.5H_2O$ which was assumed with ^1H NMR measurement.

Table 3-3. Host-guest ratio comparison for EtOH adsorbed complex **2** and **3.** The amount of adsorbed EtOH was determined by ^1H NMR spectrum and the observed remaining weight loss in thermogravimetric analysis was assumed as H_2O.

	EtOH (/ 1 complex)	H_2O (/ 1 complex)
Complex 2	1.0	1.0
Complex 3	0.7	5.5

In chapter 2, I have showed that **2** exhibited unique vapochromism with the "shape-memory" behavior; the amorphous form, **2-Pa** could be transformed to porous crystalline form by adsorption of EtOH vapor, and its crystal structure could be retained even after removal of EtOH vapor. On the other hands, PXRD measurement of **3** suggested that the porous crystal structure of **3-Oc** was less stable than **2-Rc**. To elucidate vapor adsorption process in detail, EtOH vapor adsorption isotherms were measured at 298 K. Figure 3-7 showed the EtOH adsorption isotherms of **3** compared with **2**. At the first measurement, the amorphous-like solids, **3-Ya** and **2-Pa** were used and both complexes were heated at 120 °C for 24 hours before the measurements to remove all adsorbed solvent molecules. Although **3-Ya** hardly adsorbed EtOH vapor at the low relative pressure range below ($P/P_0 < 0.6$), large amount of EtOH vapor (~1.9 mol/mol at saturated vapor pressure) was adsorbed at higher region. In the desorption process, most of the adsorbed EtOH molecules were retained even at $P/P_0 = 0.4$, and then started to be desorbed at lower pressure. This large hysteresis in the adsorption/desorption cycle is a characteristic behavior for the vapor ad/desorption which involves a significant structure transformation of the adsorbent, that is, **3-Ya** to **3-Oc**⊃EtOH. Similar hysteresis was observed for **2-Pa** as shown in Figure 3-7 (b), but **2-Pa** adsorbed EtOH vapor at lower pressure region than that of **3-Ya**. In addition, the remained EtOH in the desorption process for **3** (0.5 mol/mol) was smaller than that of **2** (0.9 mol/mol). These differences may be due to the following two reasons; the destabilized porous structure by expanded pore size and the increased hydrophobicity of the pore surface by the phenyl rings of H_2d*pc*pbpy ligand. Both complexes adsorbed almost the same amount of EtOH vapor (~2 mol/mol at the saturated vapor pressure) in spite of the different pore size, suggesting that EtOH vapor molecules were adsorbed at the specific sites in the pore. Considering that crystal water molecules were hydrogen bonded to the O atoms of the carboxy groups of H_2d*pc*pbpy ligand in **3-Oc** (see Figure 3-4), EtOH molecules are thought to be adsorbed at the similar positions by the hydrogen bonding interaction. Next, we conducted the second measurement by using the same samples which used in the first measurement. The samples were heated at 120 °C for 24 hour to remove all of the EtOH molecules adsorbed in the first measurement. As described in chapter 2, **2** showed completely different isotherm to the first cycle; large amount of EtOH adsorption at very low relative pressure (P/P_0=0.01) was observed. Such an isotherm is so-called Type I isotherm which is the characteristic feature for microporous materials. In contrast, **3** did not exhibit such the Type I isotherm in the second measurement but showed almost the identical vapor adsorption isotherm to that observed in the 1st measurement. Therefore, as suggested by PXRD measurement (See Figure 3-5), the porous structure of **3-Oc** was collapsed by desorption of EtOH molecules.

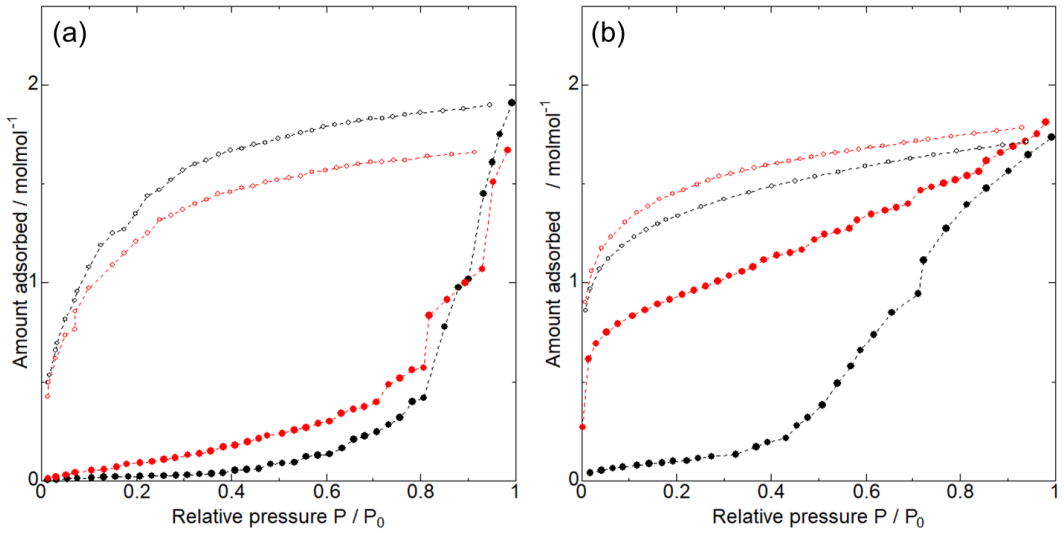

Figure 3-7. EtOH vapor adsorption isotherms of (a) **3** and (b) **2** at 298 K. The same samples were used continuously in these two measurements each other. At the first measurements (black circles), amorphous form of **3** and **2** was used. Before the second measurements (red circles), the samples were heated again at 120°C under vacuum to remove all the adsorbed vapor molecules in the first measurement.

3-3-4 Vapochromism

As mentioned in Chapter 2, the amorphous form of **2-Pa** exhibited "molecular-scale shape-memory" vapochromism because of its porous structure that adsorbed the alcoholic vapors and collapsed by manual grinding. Although the porous crystalline structure of **3-Oc** was quite similar to that of **2-Rc**, the former complex could not retain its form without the adsorbed solvent molecules. Consequently, a different chromic behavior than that shown by **2** was expected for complex **3**. To investigate this difference, solid-state UV-Vis diffuse reflectance and emission spectral changes of **3-Ya** upon vapor ad/desorption were measured. As shown in Figure 3-8, **3-Ya** showed a broad orange emission centered at 626 nm, which was over 100 nm shorter wavelength than that of **2-Pa** (733 nm). This blue-shift of the emission band is probably due to the destabilized MMLCT energy resulting from the weaker intermolecular interaction in **3-Ya** in comparison to that of **2-Pa**, as suggested by the single crystal X-ray analyses (Table 3-2) and diffuse reflectance spectra (Figure 3-8) of these complexes. The absorption band corresponding to the ^{1}MMLCT transition in **3-Ya** was observed at a shorter wavelength by about 200 nm as compared to that of **2-Pa**. The emission band maximum of **3-Ya** was blue-shifted from 626 nm to 603 nm upon exposure to EtOH vapor, which is similar to that observed in the case of **3-Oc**. PXRD analyses (Figure 3-3) also indicated the EtOH vapor adsorption-induced structural transformation from **3-Ya** to **3-Oc⊃EtOH**. On the other hand, the absorption band corresponding to the ^{1}MMLCT transition of **3-Ya** shifted drastically to a longer wavelength from 500 nm to 600 nm upon exposure to EtOH vapor. A similar red shift was also observed in the excitation spectrum; the excitation band of ^{1}MMLCT transition shifted by ~60 nm (Figure 3-9) when **3-Ya** was exposed to EtOH vapor. These red-shifted absorption and excitation bands suggest that the intermolecular Pt···Pt interactions in **3-Oc⊃EtOH** are basically stronger than those in the yellow amorphous powder, **3-Ya**. The inconsistency of these results with the blue-shifted ^{3}MMLCT transition observed in the emission spectrum of **3-Oc⊃EtOH** may be attributed to the emission from the impurity sites with shorter Pt···Pt distance in the amorphous **3-Ya** state. The amorphous powder **3-Ya** should have a larger number of structural defects as compared to the orange crystalline form **3-Oc**. Such defects in the amorphous state may enable to form small domain with the shorter Pt···Pt distance than that in the highly ordered crystalline form **3-Oc**, resulting in the lower energy emission *via* energy transfer from the other domains with longer Pt···Pt distance.

In chapter 2,the ^{3}MMLCT emission of **2-Rc⊃EtOH** exhibited a blue-shift of ~20 nm upon the removal of adsorbed EtOH vapor by heating. The ^{3}MMLCT emission wavelength was further shifted to a longer wavelength to ~700 nm after manual grinding. Similar changes were observed in the UV-Vis diffuse reflectance spectrum (Figure 3-8) and the PXRD measurements indicated that this two-step change originated from the slight structural deformation by EtOH

desorption and transformation to the amorphous powdery form by grinding (Figure 3-3). On the other hand, there was hardly any change in the diffuse reflectance spectrum of **3-Oc⊃EtOH** after the removal of the adsorbed EtOH by heating whereas the emission band maximum was significantly shifted to longer wavelengths by ~50 nm. As shown in Figure 3-3, this behavior corresponds to the collapse of the porous crystal structure upon EtOH desorption and the transformation to the orange-colored amorphous solid **3-Oa**. Considering that the ^{1}MMLCT absorption band was hardly changed (red and blue lines in Figure 3-8c), intermolecular Pt···Pt interactions in the ground state of **3-Oa** would be comparable to the crystalline form, **3-Oc**, which has the same orange color. Therefore, the red-shift of the ^{3}MMLCT presumably corresponds to the energy transfer to the impurity sites with shorter Pt···Pt distances, as discussed above for **3-Ya**. That is, the amorphous solid of **3-Oa** exhibited a larger Stokes shift (see red lines in Figures 3-8a and 3-8c) than the crystalline form **3-Oc** (see blue lines in Figures 3-8a and 3-8c) because of the larger number of structural defects that may allow to form shorter Pt···Pt distance in the stacking structure. This assumption is supported by the IR spectra of these forms (Figure 3-10); the C≡N stretching mode of **3-Oa** (2134 cm^{-1}) was observed at a very similar wavenumber to that of **3-Ya (**2135 cm^{-1}) and also at a lower frequency compared to that of **3-Oc** (2159 cm^{-1}). This lower-energy C≡N stretching mode of both the amorphous forms, **3-Ya** and **3-Oa**, suggests that the rigidity of the intermolecular hydrogen-bonded network structure of the amorphous phases **3-Ya** and **3-Oa** is weaker than that of the crystalline form **3-Oc**.

The large structural difference between the EtOH-desorbed **3-Oa** and **2-Rc** certainly affects the sensitivity of the ^{3}MMLCT emission energy for H_2O vapor in air. As shown in a previous report,[41] the ^{3}MMLCT emission of **2-Rc** was blue-shifted from 665 nm to 633 nm with the increase in relative humidity (from 11 to 100% RH), probably as a result of the physisorption of H_2O molecules into the porous channel of **2-Rc**. In contrast, the ^{3}MMLCT emission energy of the EtOH-desorbed complex **3-Oa** changed only slightly from 652 nm to 658 nm upon increasing RH in this abovementioned range (Figure 3-11). The lesser sensitivity of **3-Oa** in comparison with that of **2-Rc** is probably due to the lack of porous channels in **3-Oa**.

Interestingly, the emission and diffuse reflectance spectra of the EtOH-desorbed amorphous orange form, **3-Oa**, were remarkably blue shifted and similar to that of **3-Ya** after manual grinding. Notably, some peaks in the PXRD pattern of **3-Oa** completely disappeared after manual grinding (Figure 3-3). This result suggests that the short-range ordered domains with effective intermolecular Pt···Pt interactions in **3-Oa** could be collapsed easily and completely to form **3-Ya** by grinding.

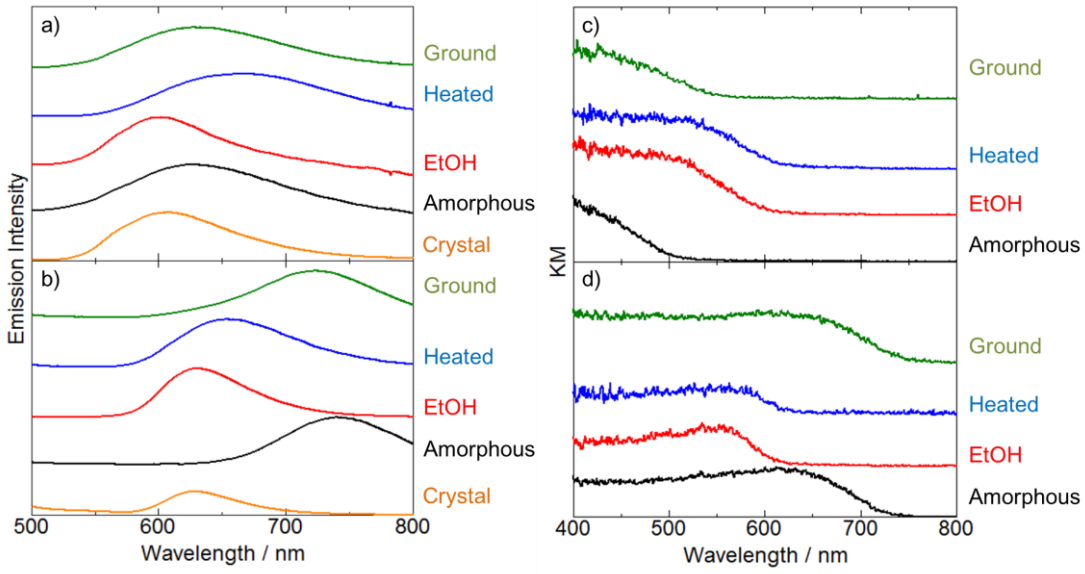

Figure 3-8. Luminescence spectrum and diffuse reflectance spectrum changes of (a,c) **3** and (b,d) **2**. The amorphous form (black line) was exposed to EtOH vapor for 5 days at 303 K (red line). Then the sample was heated to remove all EtOH (blue line). After that, the sample was ground manually by using mortar (green line). The orange lines show the luminescence spectra of the crystal.

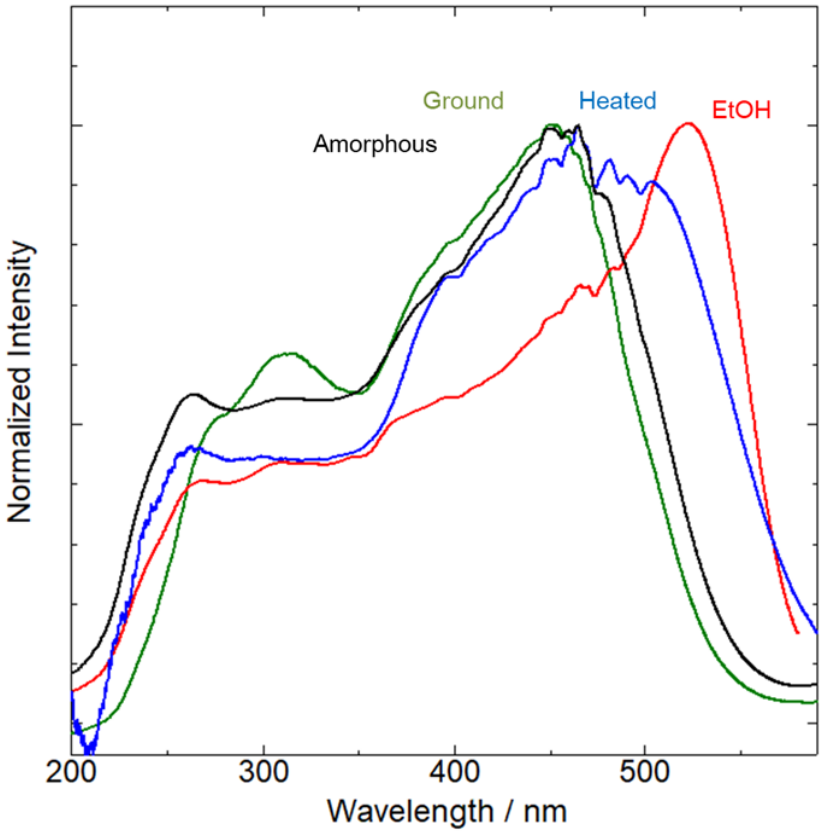

Figure 3-9. Excitation spectrum of **3**. The spectrum corresponds to the luminescence spectrum on Figure 3-8-(a). The amorphous form of **3**(**3-Ya,** black line) was exposed to EtOH vapor for 5 days (**3-Oc**, red line). After that, the sample was heated at 120°C for 3 h (**3-Oa**, blue line) and subsequently ground by using mortar (green line).

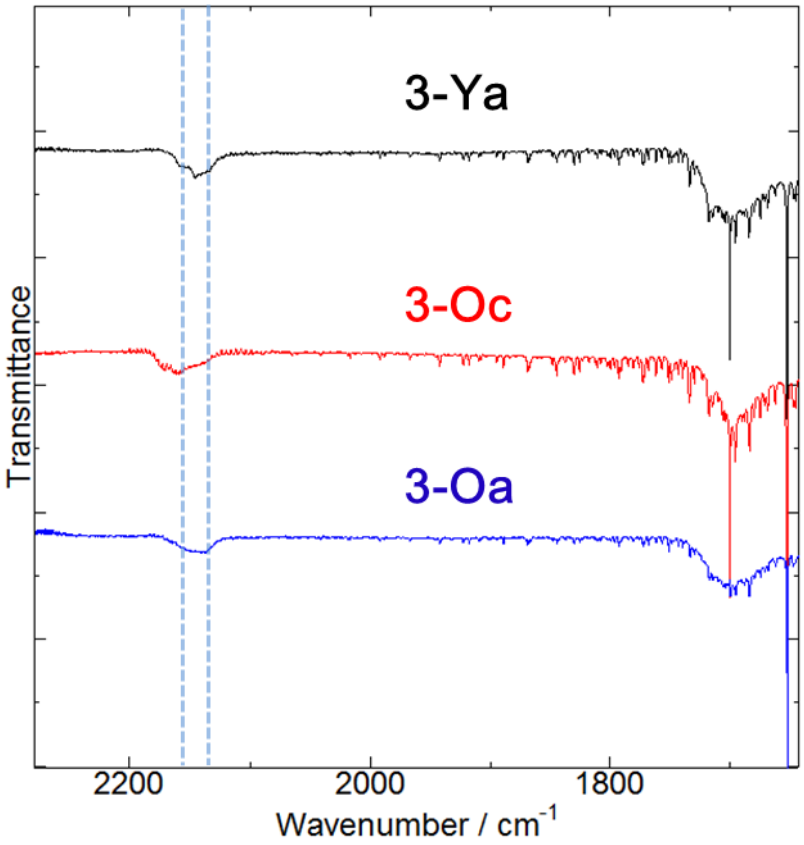

Figure 3-10. IR spectrum (ATR method) for 3-Ya(black), 3-Oc(red) and 3-Oa(blue). 3-Oc and 3-Oa were generated by adsorption and desorption of 2-PrOH vapor, because of EtOH vapor released too fast from the **3-Oc** to measure the crystalline state.

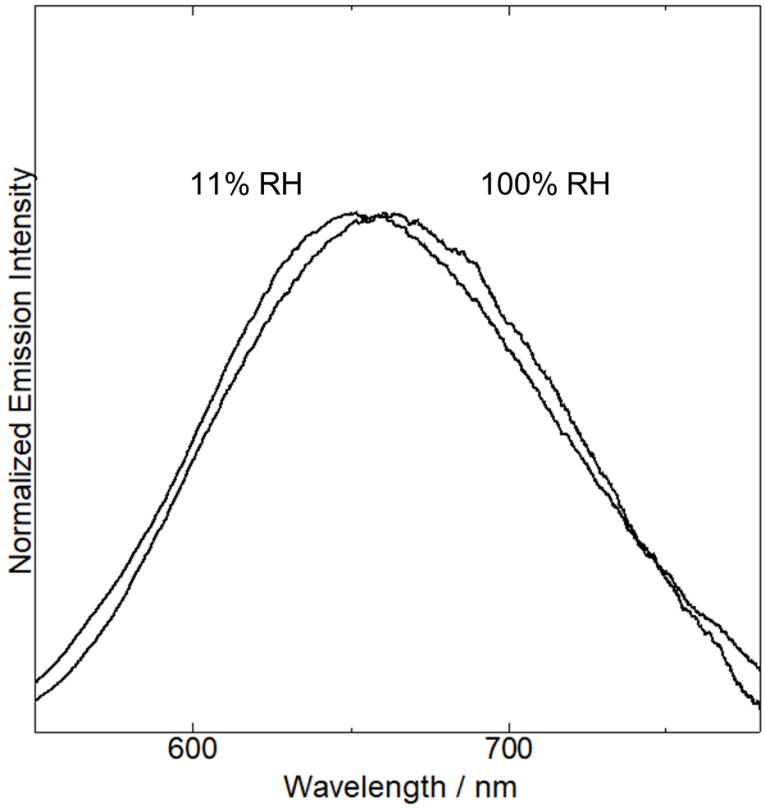

Figure 3-11. Relative humidity response of **3-Oa**. The humidity was controlled by using saturated aqueous solutions of LiCl (11%) and water (100%).[12)]

The plausible mechanism of the vapochromic behavior of complex **3** is summarized in Scheme 3-2. The as-prepared yellow-colored amorphous powder of **3**, **3-Ya**, exhibited a higher energy ^{1}MMLCT absorption band compared to the other orange-colored forms because of the weaker intermolecular Pt···Pt interactions. Upon exposure of **3-Ya** to EtOH vapor, the vapor adsorption-induced structural transformation to the orange-colored crystalline form, **3-Oc⊃EtOH** took place. In the transformation from **3-Ya** to **3-Oc⊃EtOH**, the ^{1}MMLCT absorption band clearly shifted to a longer wavelength (from 500 nm to 600 nm) while the ^{3}MMLCT emission band inversely shifted to a shorter wavelength (from 626 nm to 603 nm) as shown in Figures 3-8a and 3-8c. It may be concluded from these inverted shifts in the two spectra that there is a contribution from the impurity sites with shorter Pt···Pt distances. In the amorphous powder **3-Ya**, a lot of structural defects may allow to form shorter Pt···Pt distances microscopically, leading to the lower energy ^{3}MMLCT emission in comparison to the highly ordered crystalline form **3-Oc⊃EtOH**. Furthermore, **3-Oc⊃EtOH** can be easily transformed to the orange amorphous solid **3-Oa** by desorption of the EtOH molecules assisted by heating. During this structural change to **3-Oa**, only a negligible shift was observed in the diffuse reflectance spectrum whereas an obvious red-shift was observed in the emission spectrum. Thus, the intermolecular Pt···Pt interactions are presumably still partly effective in the amorphous form **3-Oa**. The amorphous nature of **3-Oa** and **3-Ya** is also responsible for the large Stokes shift in these complexes, i.e., the contribution of the impurity levels derived from the microscopically-formed domains with the shorter Pt···Pt distances. This can explain why only the emission spectrum was changed upon EtOH desorption.

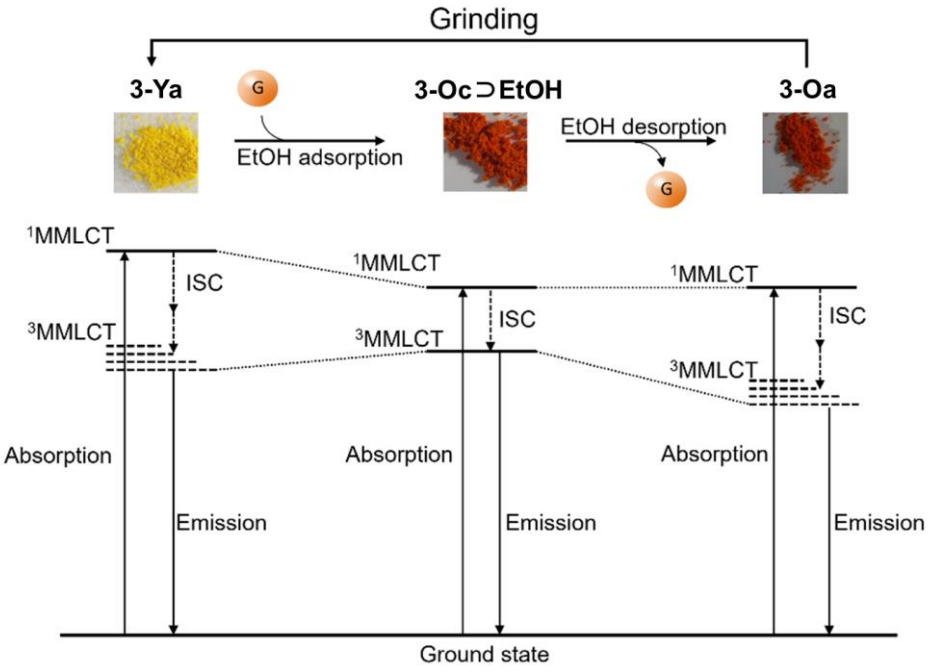

Scheme 3-2. Schematic illustration of vapochromic response for **3**. Dotted lines of ^{3}MMLCT states of **3-Ya** and **3-Oa** schematically show the contribution of various strengths of intermolecular Pt···Pt distances in amorphous states.

3-4 Conclusion

A new luminescent Pt(II) complex, $[Pt(CN)_2(H_2dpcpbpy)]$ (**3**; $H_2dpcpbpy$ = 4,4'-*p*-dicarboxyphenyl-2,2'-bipyridine) was successfully synthesized. The orange crystal of **3-Oc** was identified to be the isomorphous porous form of the red crystalline form **2-Rc**, $[Pt(CN)_2(H_2dcphen)]$ (**2**, $H_2dcphen$ = 4,7-dicarboxy-1,10-phenanthroline). The porous structure was constructed by the 2-D hydrogen bonding network in the *ab* plane and the effective intermolecular Pt···Pt interaction along the *c* axis. As expected from the molecular structure of **3**, **3-Oc** had a larger pore size and void fraction than that of **2-Rc**.

The as-synthesized yellow amorphous solid **3-Ya** exhibited a completely different color from the as-synthesized purple amorphous form **2-Pa**. This is because of the weaker intermolecular Pt···Pt interaction competing with the π-π stacking interactions of the expanded π plane of the ligand. **3-Ya** exhibited vapor induced color change as a result of the reversible EtOH vapor adsorption and desorption, which induced structural transformation between the amorphous **3-Ya** and the porous crystalline **3-Oc** states. Moreover, EtOH vapor exposed **3** adsorbed much more molecules than EtOH vapor exposed **2**. This difference is probably due to the expanded pore size. Although this vapor induced structural change of **3** was similar to that of **2**, the vapor adsorption isotherms and PXRD measurements revealed that the porous crystal structure of **3-Oc** could not be retained after the removal of EtOH vapor by heating. In contrast, **2-Rc** could retain its porous structure without the adsorbed EtOH. This difference is probably due to the larger void fraction and weaker intermolecular hydrogen bonding interactions in **3-Oc** than **2-Rc**, as suggested by their crystal structures.

On the other hand, after the desorption of EtOH, **3-Oa** exhibited a very similar diffuse reflectance spectrum to that of **3-Oc**. This behavior could be explained by the small crystal domains with the effective Pt···Pt interactions that still remained in **3-Oa**. Moreover, upon these processes, a larger Stokes shift was observed for the amorphous form **3-Oa** as compared to the crystalline form **3-Oc**. This difference may be a result of the impurity sites with shorter Pt···Pt distances. In the amorphous form, loosely packed molecules could form the small domains with shorter Pt···Pt distances than in the dense packed crystalline form **3-Oc**. The emission spectrum of **3-Oa** was hardly affected by water vapor in air whereas the ^{3}MMLCT emission band of **2-Rc** was moderately shifted by the physisorbed water vapor. In other words, the existence of the porous structure of **2-Rc** is a key factor in the sensitivity toward water. Furthermore, **3-Oa** could be transformed to the initial **3-Ya** form by manual grinding. This was probably caused by the collapse of the small crystalline domains with the effective Pt···Pt interaction upon grinding. Therefore, **3** exhibited vapor history sensing ability because of its partially retained Pt···Pt interactions after the collapse of the porous structure. **3-Oa** also showed negligible humidity-dependent luminescence because it lacked the porous structure. Thus, **3** would be a

more promising vapor history sensor than complex **2** because of its lack of sensitivity for water vapor in air.

3-5 References

(1) a) C. E. Strasser and V. J. Catalano, *J. Am. Chem. Soc.*, **2010**, *132*, 10009-10011. b) J. Ni, X. Zhang, Y.-H. Wu, L.-Y. Zhang and Z.-N. Chen, *Chem. Eur. J.*, **2011**, *17*, 1171-1183. c) S. H. Lim, M. M. Olmstead and A. L. Balch, *J. Am. Chem. Soc.*, **2011**, *133*, 10229-10238. d) S. J. Choi, J. Kuwabara, Y. Nishimura, T. Arai and Takaki Kanbara, *Chem. Lett.*, **2012**, *41*, 65-67. e) X. Zhang, J.-Y. Wang, J. Ni, L.-Y. Zhang and Z.-N. Chen, *Inorg. Chem.*, **2012**, *51*, 5569-5579. f) Y. Li, L. Chen, Y. Ai, E. Y.-H. Hong, A. K.-W. Chan and V. W.-W. Yam, *J. Am. Chem. Soc.*, **2017**, *139*, 13858-13866.

(2) Y. Shigeta, A. Kobayashi, T. Ohba, M. Yoshida, T. Matsumoto, H.-C. Chang and M. Kato, *Chem. Eur. J.*, **2016**, *22*, 2682-2690.

(3) Y. Sakata, S. Furukawa, M. Kondo, K. Hirai, N. Horike, Y. Takashima, H. Uehara, N. Louvain, M. Meilikhov, T. Tsuruoka, S. Isoda, W. Kosaka, O. Sakata and S. Kitagawa, *Science*, **2013**, *339*, 193-196.

(4) D. Zhang, E. J. Dufek, E. L. Clenna, *J. Org. Chem.*, **2006**, *71*, 315-319.

(5) P. Kavanagh and D. Leech, *Tetrahedron Lett.*, **2004**, *45*, 121-123.

(6) W.-S. Han, J.-K. Han, H.-Y. Kim, M. J. Choi, Y.-S. Kang, C. Pac and S. O. Kang, *Inorg. Chem.,* **2011**, *50*, 3271–3280

(7) P. Kurach, S. Luliński, and J. Serwatowski, *Eur. J. Org. Chem.* **2008**, 3171–3178.

(8) D. R. Coulson, L. C. Satek and S. O. Grim, *Inorg. Synth.*, **1972**, *13*, 121.

(9) M. Kato, S. Kishi, Y. Wakamatsu, Y. Sugi, Y. Osamura, T. Koshiyama and M. Hasegawa, *Chem. Lett.* **2005**, *34*, 1368-1369.

(10) Crystal Clear: Data Collection and Processing Software, Rigaku Corporation, 1998-2014, Tokyo, Japan.

(11)SHELXS2013 and SHELXL2013: G. M. Sheldrick, *Acta Cryst.*, **2008**, A64, 112-122.

(12) H. L. Goderis, B. L. Fouwe, S. M. Van Cauwebergh and P. P. Tobback, *Anal. Chem.* **1986**, *58*, 1561-1563.

Chapter 4

General Conclusion

General Conclusion

In this thesis, vapochromic behavior and the structural stability of porous Pt(II) complexes constructed by 2-D hydrogen bonding network and Pt-Pt interactions were described.

In chapter 1, my research background particularly about vapochromism, porous material and purpose of the thesis were briefly described.

In chapter 2, a porous luminescent complex, $[Pt(CN)_2(H_2dcphen)]$ (**2**; H_2dcphen = 4,7-dicarboxy-1,10-phenanthroline) was synthesized and its luminescence property was investigated in detail to compare with that of the previously reported analogue, $[Pt(CN)_2H_2dcbpy]$ (**1**; H_2dcbpy = 4,4'-dicarboxy-2,2'-bipyridine). The amorphous form of **2** exhibited vapochromism upon exposure to alcoholic vapor which was originated from the vapor-adsorption-induced amorphous to porous crystalline transformation. Moreover, the smaller pore size of **2** (6.4×6.8 $Å^2$) than **1** (6.1×8.8 $Å^2$) improved the vapor selectivity in the vapochromic behavior; **1** exhibited amorphous to crystalline transformation upon exposure to the ranging from MeOH to *t*-BuOH, whereas t-BuOH vapor did not induce the transformation of **2**. The porous structure of **2** was found to be stable without adsorbed vapor molecules in the pore. This stable porous structure of **2R** enables it to detect H_2O vapor which could not induce the transformation. In addition, the initial purple amorphous form was recovered by manual grinding. This unique "molecular-scale shape-memory" behavior in vapochromic process based on the stable porous structure enabled **2** to memorize the past vapor adsorption.

In chapter 3, to examine the extensibility and stability of porous structures of **1** and **2**, a luminescent Pt (II) complex $[Pt(CN)_2(H_2d\textit{p}cpbpy)]$ (**3** ; $H_2d\textit{p}cpbpy$ = 4,4'-di(*p*-carboxyphenyl)-2,2'-bipyridine) was synthesized and its vapochromic behavior was evaluated by various measurements. The porous orange crystalline form of **3**, **3-Oc** was isomorphous to **2-Rc** and slightly weaker but effective Pt-Pt interaction than **2-Rc** was observed. Notably, **3-Oc** had a larger pore (14.3 × 8.6 $Å^2$) and void fraction (48.7%) than that of **2-Oc (**6.4 × 6.8 $Å^2$, 35.2%**)**, because of newly introduced phenyl ring between the bpy moiety and the carboxy group. **3** also exhibited similar vapochromism to that of **2** which originates from the structural transformation between the amorphous and porous crystal phases. Although the porous structure of **3-Oc** could not be retained without adsorbed vapor molecules probably because of the larger pore and weaker intermolecular hydrogen bonds, the color was almost unchanged after the removal of adsorbed EtOH molecules. The original yellow-colored amorphous-like form was recovered by manual grinding of the vapor-removed amorphous-like form.

In this thesis, Type I vapochromism with porous supramolecular structure constructed by hydrogen bonding was investigated by systematically modification of previously reported $[Pt(CN)_2(H_2dcbpy)]$. Obtained complexes transformed to slightly different various crystal

structures by external stimuli, probably due to the flexibile hydrogen bonding. Moreover, each form could be distinguished as their absorption and/or emission by sensitive Type I mechanism. Although it is still difficult to control crystal structure and external stimuli responsiveness, Type I mechanism with hydrogen bonded supramolecular porous structures are expected to be good candidate for multi-functional smart materials.

Acknowledgement

This study on this thesis has been carried out under the direction of Professor Masako Kato during April 2013-March 2018 at the Graduate School of Chemical Sciences and Engineering, Hokkaido Universiy.

I owe my deepest gratitude to Professor Masako Kato for her earnest guidance and invaluable suggestions. I am also deeply grateful to Associate Professor Atsushi Kobayashi for his proper suggestions and wide-ranging guidance. I would like to express my gratitude to Professor Ho-Chol Chang (present address, Chuo University), Assistant Professor Masaki Yoshida and Assistant Professor W. M. C. Sameera for invaluable discussions and comments. I would like to deepest appreciation to Professor Kazuki Sada, Professor Takanori Suzuki and Professor Yasuchika Hasegawa for reviewing this thesis. I would like to offer my special thanks to Professor Reiji Kumai, Associate Professor Sagayama Hajime and Mr. Yasuhiro Niwa for X-ray diffraction measurements using synchrotron at Photon Factory, KEK.

I am thankful to Ms. Mayu Shimizu, Ms. Mariko Tsukada and Ms. Yuriko Zeff for secretarial works. I would like to thank Dr. Takeshi Matsumoto, Dr. Masanori Wakizaka, Dr. Tadashi Ohba, Dr. Hiroki Ohara, Dr. Erika Saitoh, Dr. Kana Sato and Dr. Tomohiro Ogawa for kind comments and encouragements. Special thanks also to all members of the group of Professor Kato for their friendship during the time in the laboratory.

This work was supported by the Grant-in-Aid for JSPS Research Fellow (17J01139).

Finally, I would like to express special thanks to my parents, sister, and friends for their supports and encouragement.

Yasuhiro Shigeta

Graduate School of Chemical Sciences and Engineering